remote sensing

MDPI

Article

# Performance of the Atmospheric Radiative Transfer Simulator (ARTS) in the 600–1650 cm$^{-1}$ Region

**Zichun Jin [1], Zhiyong Long [2], Shaofei Wang [2] and Yunmeng Liu [1,*]**

[1] Shanghai Institute of Technical Physics, Chinese Academy of Sciences, Shanghai 200083, China; jinzichun@mail.sitp.ac.cn
[2] College of Meteorology and Oceanography, National University of Defense Technology, Changsha 410037, China; longzhiyong17@nudt.edu.cn (Z.L.); wangshaofei23@nudt.edu.cn (S.W.)
* Correspondence: liuyunmeng@mail.sitp.ac.cn

**Abstract:** The Atmospheric Radiative Transfer Simulator (ARTS) has been widely used in the radiation transfer simulation from microwave to terahertz. Due to the same physical principles, ARTS can also be used for simulations of thermal infrared (TIR). However, thorough evaluations of ARTS in the TIR region are still lacking. Here, we evaluated the performance of ARTS in 600–1650 cm$^{-1}$ taking the Line-By-Line Radiative Transfer Model (LBLRTM) as a reference model. Additionally, the moderate resolution atmospheric transmission (MODTRAN) band model (BM) and correlated-k (CK) methods were also used for comparison. The comparison results on the 0.001 cm$^{-1}$ spectral grid showed a high agreement (sub-0.1 K) between ARTS and LBLRTM, while the mean bias difference (MBD) and root mean square difference (RMSD) were less than 0.05 K and 0.3 K, respectively. After convolving with the spectral response functions of the Atmospheric Infra-Red Sounder (AIRS) and the Moderate Resolution Imaging Spectroradiometer (MODIS), the brightness temperature (BT) differences between ARTS and LBLRTM became smaller with RMSDs of <0.1 K. The comparison results for Jacobians showed that the Jacobians calculated by ARTS and LBLRTM were close for temperature (can be used for Numerical Weather Prediction application) and $O_3$ (excellent Jacobian fit). For the water vapor Jacobian, the Jacobian difference increased with an increasing water vapor content. However, at extremely low water vapor values (0.016 ppmv in this study), LBLRTM exhibited non-physical mutations, while ARTS was smooth. This study aims to help users understand the simulation accuracy of ARTS in the TIR region and the improvement of ARTS via the community.

**Keywords:** Line-By-Line; radiative transfer model; ARTS; LBLRTM; thermal infrared

check for updates

**Citation:** Jin, Z.; Long, Z.; Wang, S.; Liu, Y. Performance of the Atmospheric Radiative Transfer Simulator (ARTS) in the 600–1650 cm$^{-1}$ Region. *Remote Sens.* **2023**, *15*, 4889. https://doi.org/10.3390/rs15194889

Academic Editor: Carmine Serio

Received: 24 August 2023
Revised: 28 September 2023
Accepted: 7 October 2023
Published: 9 October 2023



## 1. Introduction

With the development of satellite remote sensing applications, radiative transfer models (RTMs) have become indispensable, including satellite observation calibration [1–3], physical retrievals from satellite observations [4], and data assimilations in numerical weather prediction (NWP) models [5]. The most accurate model to calculate the absorption coefficients is the Line-By-Line (LBL) Model [6]. It calculates the absorption coefficients at an arbitrary wavenumber by integrating pressure- and temperature-dependent absorption lines provided by spectroscopic databases (e.g., high-resolution transmission molecular absorption database, HITRAN [7–9]) with relatively high computational resources [10]. Additionally, some models have simplified the calculation of absorption coefficients by transferring LBL's high-spectral-resolution absorption into average integrated strength, including the band model (BM) and correlated-k (CK) method [11–13]. Others built look-up tables [14] or directly established regression relationships between the absorption coefficients and the predictors (e.g., temperature, $H_2O$, and $CO_2$) [15,16]. The latter two can be collectively called the fast models. Fast models have a higher calculation efficiency at the expense of accuracy. In recent years, there have still been emergences of new RTMs or the

addition of new features of commonly used RTMs in the community, such as the Advanced Radiative Transfer Modeling System (ARMS, a new generation of the fast radiative transfer model developed for NWP and remote sensing applications) [17] and moderate resolution atmospheric transmission-6 (MODTRAN6, a new LBL option has been developed) [18,19].

In this study, the protagonist of our investigation is the Atmospheric Radiative Transfer Simulator (ARTS) [20–22]. ARTS is an open-source LBL RTM designed for the millimeter and sub-millimeter spectral range developed by Universität Hamburg and Chalmers University. The main advantages of ARTS include (1) the fact it is a 3D radiation transfer model; (2) it supports the calculation of one to four Stokes components (i.e., polarized radiative transfer calculations); (3) it has a highly modular design allowing users to control the simulation settings in a more straightforward manner, e.g., selecting the type of gas considered in the simulation and deciding whether to calculate the Jacobian and instrument response through options. Nowadays, ARTS is widely used in the simulation of the microwave–terahertz spectrum [23–25]. Eriksson et al. [23] built an operational ice cloud product inversion algorithm based on ARTS for the upcoming terahertz ice cloud imager. Bobryshev et al. [24] compared the simulated radiosonde data with the 183.31 GHz brightness temperature based on ARTS with a mean bias of 0.4 K (smaller than previous studies). Barlakas et al. [25] evaluated the Radiative Transfer for TOVS-Scatt (RTTOV-SCATT) using ARTS as a reference and found that as the scattering increases, the $\delta$-Eddington solution used by the RTTOV-SCATT failed to produce sufficient brightness temperature depressions. Moreover, due to the same physical principles (radiation sources include emissions from the Earth's surface and the atmosphere), ARTS can also be used for simulations in the thermal infrared (TIR) region [26,27]. So far, the performance of ARTS in the microwave region has been well validated and intercompared [6,24,28–30], while its capability in TIR has received little attention. An intercomparison was made by Saunders et al. [31] between ARTS v1 and other RTMs (both LBL models and fast models) over Atmospheric Infra-Red Sounder (AIRS) channels. The results showed that ARTS exhibited similar accuracy to the remaining LBL models with a bias of 0.02 K and a standard deviation of 0.07 K averaged over 49 diverse profiles across all AIRS channels. However, ARTS showed a relatively more significant difference with a standard deviation of 0.2 K in the 650–770 $cm^{-1}$ and 2350–2423 $cm^{-1}$ spectral range. Schreier et al. [30] used ARTS v2.2 for an intercomparison with two other LBL models in High-resolution Infra-Red Sounder-like (HIRS-like) spectral channels. The agreement was better than 0.1 K in some window channels, while the discrepancies were about 0.5 K when averaged over all atmospheres, primarily due to the choice of the continuum used. However, one should keep in mind that the channel bandwidths of HIRS are greater than 10 $cm^{-1}$, with only one exception: the 15 µm channel with a bandwidth of 2.5 $cm^{-1}$. Therefore, the performance of ARTS at a higher spectral resolution (e.g., 0.001 $cm^{-1}$) has not been carefully investigated and evaluated. In addition, the latest ARTS pre-release version is 2.5.10. Compared to ARTS v2.2, the radiative transfer code was totally revised, and some new features (e.g., new versions of the continuum model) were updated. Therefore, further work is still needed to investigate the performance of the latest version of ARTS in the TIR region.

Solar radiation was not considered in this study due to the ability of ARTS to handle solar radiation is still under development [21]. The spectral range for the simulation was 600–1650 $cm^{-1}$ for two reasons: (1) the contribution of solar radiation is negligible in this range; (2) this spectral range is commonly used for infrared imager (IR-I) and infrared sounder (IR-S) channels due to both the atmospheric window and various gas absorption lines (e.g., $CO_2$, $H_2O$, and $O_3$) being contained [32].

The Line-By-Line Radiative Transfer Model (LBLRTM) is an accurate RTM which can be used over the full spectral range (i.e., from the microwave to the ultraviolet) [10,33]. LBLRTM is classical and at the leading edge of the field [34]. On the one hand, LBLRTM has been validated not only against the simulation results of other RTMs [35,36], but also the high-resolution spectral measurements [37–39]. On the other hand, LBLRTM has been widely used as the foundation for retrieval algorithms [40–42] (e.g., Infrared Atmospheric

Sounding Interferometer, IASI) and to generate the training dataset of fast models [43,44] (e.g., generating the RTTOV coefficient files from visible to infrared (IR)). Because of these advantages, the LBLRTM was selected as a reference to evaluate the performance of ARTS in the TIR region. Note that ARTS and LBLRTM both use the LBL method to solve the radiative transfer equation. For a fair comparison, we tried to ensure that the inputs to LBLRTM and ARTS were the same in our experimental setup. However, LBLRTM uses the accelerated LBL method to calculate the spectral radiance which may result in slight brightness temperature (BT) differences from ARTS.

Additionally, MODTRAN was also used for comparison. MODTRAN is the United States Air Force (USAF) standard moderate spectral resolution RTM. It was widely used for the radiative transfer simulation of IR-I instruments, such as the Moderate Resolution Imaging Spectroradiometer [45] (MODIS, onboard Terra and Aqua), Advanced Spaceborne Thermal Emission and Reflection Radiometer [46] (ASTER, onboard Terra), and the Thermal Infra-Red Sensor [47] (TIRS, onboard Landsat-8). MODTRAN5 includes two methods to calculate the absorption coefficient (BM and CK) and supports four spectral resolutions (0.1, 1, 5, and 15 $cm^{-1}$) [48].

This paper is organized in six sections: Section 2 introduces the datasets used in this study. The theory (including the radiation transfer theory and Jacobian) and experiment setup are described in Section 3. Sections 4 and 5 are the comparison results and discussion, respectively. Section 6 summarizes the work.

## 2. Datasets

### 2.1. Atmospheric Profiles

In this study, an NWP model profile dataset released by the European Organisation for the Exploitation of Meteorological Satellites (EUMETSAT) [49,50], which was used as the training dataset to calculate the coefficients for the RTTOV, was selected to evaluate the performances of ARTS. There are 83 diverse profiles contained in the profile dataset, and each profile is divided into 101 layers interpolated from the 91 levels of the profile dataset. The atmospheric pressure ranges from 1100 to 0.005 hPa, and the corresponding altitude is calculated based on the hydrostatic equilibrium (i.e., 0 to 74.05 km). In addition to the atmospheric temperature, the profiles record each layer's volume mixing ratios of six gases ($H_2O$, $CO_2$, $O_3$, $N_2O$, CO, and $CH_4$, all in ppmv). The statistical characteristics of temperature and the six gases are shown in Figure 1. For $H_2O$, the range of the total column content is $3.87 \times 10^{-3}$ to $1.06 \times 101$ g/cm$^2$; for $CO_2$, the range is 0.571 to 0.743 g/cm$^2$; for $O_3$, the range is $9.23 \times 10^{-5}$ to $1.69 \times 10^{-3}$ g/cm$^2$; for $N_2O$, the range is $4.73 \times 10^{-4}$ to $5.46 \times 10^{-4}$ g/cm$^2$; for CO, the range is $3.22 \times 10^{-5}$ to $3.31 \times 10^{-4}$ g/cm$^2$; and for $CH_4$, the range is $1.15 \times 10^{-5}$ to $1.18 \times 10^{-3}$ g/cm$^2$. The temperature range of the lowest layer is 211.06 to 318.26 K. Note that profiles 81 and 82 are envelopes of minimum and maximum values, and profile 83 is the mean value. The dataset can be downloaded from https://nwp-saf.eumetsat.int /site/software/atmospheric-profile-data/ (accessed on 15 July 2023).

### 2.2. Instrument Spectral Response Functions

The IR-I has a wider bandwidth than IR-S (e.g., 0.3 μm for MODIS band 33 and 0.5–2 $cm^{-1}$ for AIRS). To evaluate the performances of ARTS for both IR-I and IR-S applications, AIRS (for IR-S) and MODIS (for IR-I) onboard the Aqua satellites of the Earth Observing System (EOS) series of the National Aeronautics and Space Administration (NASA) were selected.

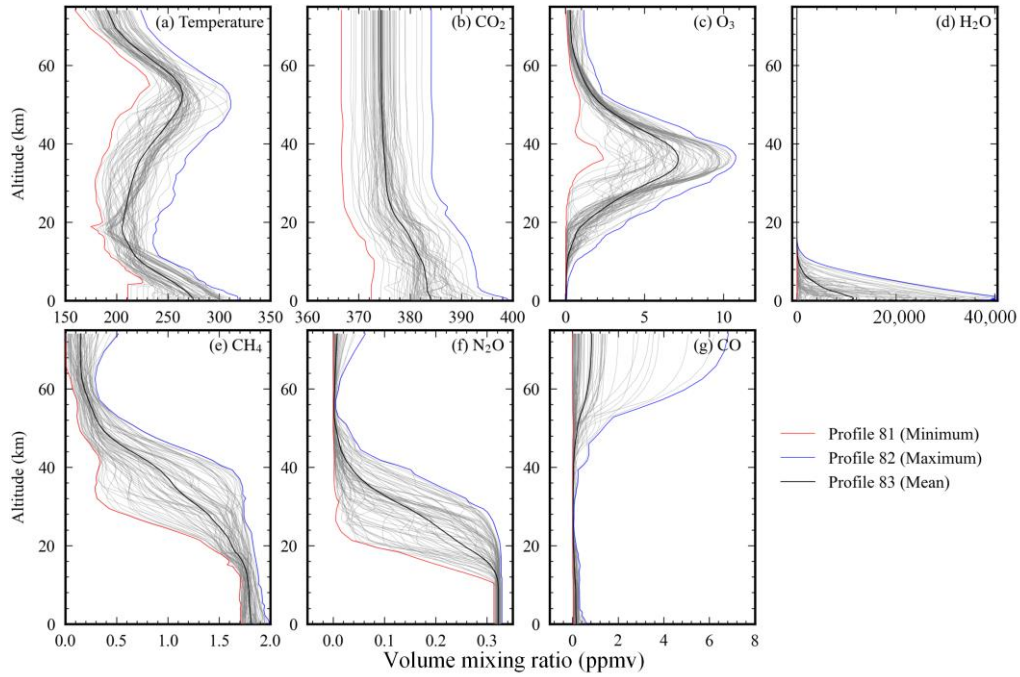


**Figure 1.** The distribution of (**a**) atmospheric temperature and (**b**–**g**) six gases of the 83 profiles as a function of altitude.

MODIS is an imaging spectroradiometer concept instrument, and its scanning method is cross-track scanning with a ±55° field of view [51]. For diagnostics of the Earth's land, ocean, and atmosphere, MODIS contains 36 bands from 0.4 to 14.5 μm with spatial resolutions of 250 m (Band1 and Band 2), 500 m (Band 3 to Band 7), and 1000 m (Band 8 to Band 36) at the nadir. In this study, ten bands (i.e., Band 27 to Band 36) located in the 600–1650 $cm^{-1}$ range were selected to evaluate the performances of the IR-I instrument. The information on the selected bands is shown in Table 1. The range of the central wavelength for the selected ten bands is 6.715–14.235 μm, and the corresponding center wavenumber range is 702.49–1489.20 $cm^{-1}$. The MODIS spectral response functions were downloaded from https://nwpsaf.eu/downloads/rtcoef_rttov12/ir_srf/ rtcoef_eos_1_modis_srf.html (accessed on 15 July 2023).

**Table 1.** Details of the selected 10 MODIS bands. NEΔT denotes noise equivalent differential temperature.

| Band Number | Central Wavelength (μm) | Central Wavelength ($cm^{-1}$) | Bandwidth (μm) | NEΔT @Specified Input | Primary Use |
|---|---|---|---|---|---|
| 27 | 6.715 | 1489.203 | 0.360 | 0.25 K @ 1.16 $W{\cdot}m^{-2}{\cdot}sr^{-1}{\cdot}\mu m^{-1}$ | Cirrus clouds andWater vapor |
| 28 | 7.325 | 1365.188 | 0.300 | 0.25 K @ 1.16 $W{\cdot}m^{-2}{\cdot}sr^{-1}{\cdot}\mu m^{-1}$ | |
| 29 | 8.550 | 1169.591 | 0.300 | 0.25 K @ 1.16 $W{\cdot}m^{-2}{\cdot}sr^{-1}{\cdot}\mu m^{-1}$ | Cloud properties |
| 30 | 9.730 | 1027.749 | 0.300 | 0.25 K @ 1.16 $W{\cdot}m^{-2}{\cdot}sr^{-1}{\cdot}\mu m^{-1}$ | Ozone |
| 31 | 11.030 | 906.618 | 0.500 | 0.05 K @ 1.16 $W{\cdot}m^{-2}{\cdot}sr^{-1}{\cdot}\mu m^{-1}$ | Surface/cloud temperature |
| 32 | 12.020 | 831.947 | 0.500 | 0.05 K @ 1.16 $W{\cdot}m^{-2}{\cdot}sr^{-1}{\cdot}\mu m^{-1}$ | |
| 33 | 13.335 | 749.906 | 0.300 | 0.25 K @ 1.16 $W{\cdot}m^{-2}{\cdot}sr^{-1}{\cdot}\mu m^{-1}$ | Cloud top altitude |
| 34 | 13.635 | 733.407 | 0.300 | 0.25 K @ 1.16 $W{\cdot}m^{-2}{\cdot}sr^{-1}{\cdot}\mu m^{-1}$ | |
| 35 | 13.935 | 717.618 | 0.300 | 0.25 K @ 1.16 $W{\cdot}m^{-2}{\cdot}sr^{-1}{\cdot}\mu m^{-1}$ | |
| 36 | 14.235 | 702.494 | 0.300 | 0.35 K @ 1.16 $W{\cdot}m^{-2}{\cdot}sr^{-1}{\cdot}\mu m^{-1}$ | |

AIRS is a high-resolution sounder that includes an IR spectrometer and a visible and near-infrared sensor [52]. Its vertical and horizontal spatial resolutions are 1 km and 13.5 km

(at nadir), respectively, with a scan of ±49.5° off-nadir. The IR spectrometer has 2378 channels, which can be divided into three spectral ranges (i.e., 3.74–4.61 μm, 6.20–8.22 μm, and 8.80–15.4 μm, see Table 2). Only the latter two spectral ranges, located in 600–1650 $cm^{-1}$, and containing 1864 channels, were selected in this study. The corresponding center wavenumber of these 1864 channels ranges from 649.62 to 1613.88 $cm^{-1}$. The AIRS spectral response functions can be downloaded from http://asl.umbc.edu/pub/airs/srf (accessed on 15 July 2023).

**Table 2.** Details of the AIRS IR spectrometer channels. NEΔT denotes the noise equivalent differential temperature.

| Spectral Range (μm) | Spectral Range ($cm^{-1}$) | Channel Number | Spectral Resolution ($cm^{-1}$) | NEΔT @Specified Input |
|---|---|---|---|---|
| 3.74–4.61 | 2170–2674 | 514 | ~2.0 | 0.14 K @ 280 K |
| 6.20–8.22 * | 1216–1613 * | 602 | ~1.0 | 0.20 K @ 280 K |
| 8.80–15.4 * | 650–1136 * | 1262 | ~0.5 | 0.35 K @ 280 K |

Note: * represents the selected spectral ranges.

## 3. Theory and Experiment Setup

### 3.1. Radiative Transfer Theory

Neglecting the contribution of solar radiation and the scattering effect, the clear-sky radiative transfer through the atmosphere can be described by a simple differential equation when the local thermodynamic equilibrium holds [20]:

$$\frac{dI(v,s)}{ds} = -\alpha(v,s)I(v,s) + \alpha(v,s)B(v,T(s)) \tag{1}$$

where $I$ denotes the radiant intensity; $v$ denotes the wavenumber; $s$ denotes the distance of the path along which the radiation travels; $\alpha$ denotes the absorption coefficient; $B$ represents the Plank function; and $T$ denotes the temperature in K.

It is evident from Equation (1) that the absorption coefficient $\alpha$ is crucial, for it appears in every term on the right side of the equation and describes the ability of all gases to absorb and emit along the propagation path. Generally, $\alpha$ is calculated as a sum of absorption lines and continuums of the different gases [53–55]:

$$\alpha = \sum_{i=1}^{N} \frac{px_i}{k_B T} \sum_{j=1}^{M_i} S_{ij}(T)F(v_{ij}) + C_1 + \ldots + C_L \tag{2}$$

where $p$ denotes the pressure; $N$ is the number of gases considered; $x_i$ represents the volume mixing ratio of the *i-th* gas; $k_B$ is Boltzmann's constant; $T$ denotes the temperature in K; $S_{ij}$ is the line strength that measures the total absorption of a spectral line and is equal to the integral over the entire spectrum; $F(v_{ij})$ is the line shape function, and $v_{ij}$ is the line center frequency; $C_1$ to $C_L$ are continuous absorptions. The line shape profile and line cutoff were used in this study, which can affect the line shape function [20].

### 3.2. Jacobian

One key usage of RTMs is to calculate top-of-atmosphere (TOA) radiances and atmospheric transmittance. Meanwhile, the gradients of the RTM radiances concerning the profile variables, denoted as the Jacobians (also called the weighting functions), are also significant, for they are the basis of the profile retrieval using satellite observations. The forward model can be expressed by Equation (3) [56,57]:

$$y = F(x) + \varepsilon \tag{3}$$

where $y$ is the measurement vector; $F$ is the forward model; $x$ is the state vector; and $\varepsilon$ is the measurement noise. Then, the Jacobian matrix $\boldsymbol{K}$ can be expressed as

$$\mathbf{K} = \frac{\partial F}{\partial x} \tag{4}$$

There are two methods to calculate the Jacobians: the first is the perturbation method, and the second is the analytical method. The perturbation method adds a small perturbation to the inverted state parameter and then calculates $\boldsymbol{K}$ using the following equation:

$$\mathbf{K} = \frac{F(x_1, \cdots x_p + \Delta x_p, \cdots) - F(x_1, \cdots x_p, \cdots)}{\Delta x_p} \tag{5}$$

where $x_p$ is the parameter of interest, and $\Delta x_p$ is the perturbation. The analytical method computes the Jacobians by deriving an analytic expression. The analytical method is faster and more accurate than the perturbation method. Currently, both LBLRTM and ARTS support the calculation of analytic Jacobians. ARTS can calculate radiance and Jacobians simultaneously, while a pre-run is required to obtain the optical depth files. However, MODTRAN5 can only calculate the Jacobians by using the perturbation method [58]. Therefore, the comparison of Jacobians was only performed between ARTS and LBLRTM.

### 3.3. Experimental Setup

In this study, five gases were taken into account in the radiative transfer simulations, including $H_2O$, $CO_2$, $O_3$, $N_2O$, and $CH_4$. CO was excluded because no CO absorption line exists in 600–1650 cm$^{-1}$. The NWP 101-level profiles mentioned in Section 2.1 were used to characterize the atmospheric condition. The surface temperature was set to the atmospheric temperature of the profile's lowest layer, and the surface emissivity was set to 0.99 [31]. The sensor position was set to the altitude of the profile's highest layer (i.e., 74.05 km). All simulations were performed under clear-sky conditions.

LBLRTM v12.15.1 (latest release version) and ARTS v2.5.10 (latest pre-release version) were selected for radiative transfer simulations. LBL models require line parameters and continuums to calculate the absorption coefficients. LBLRTM uses line parameters from the AER Line File Parameter Database (v3.8.1), which starts with HITRAN line parameters and is then modified with observed parameters [7,8]. The AER's official Binary Line File Generator (LNFL) was used to convert the AER Line File Parameter Database to the format needed for the LBLRTM. Although the simulated spectral range was 600–1650 cm$^{-1}$, we extended the spectral range by 100 cm$^{-1}$ on both sides when separating the absorption lines to ensure that all absorption lines that affected the simulated spectrum were separated. The same line parameters were also used for ARTS. The line shape profile used in this study was the Voigt profile, and the line cutoff distance was 25 cm$^{-1}$ [26]. Note that LBLRTM supports line mixing [59,60] when the line cutoff is on and off. However, ARTS only supports line mixing when the line cutoff is off. Therefore, line mixing was turned off in this study for a fair comparison (the impact of line mixing is further discussed in Section 6). The MT_CKD (Mlawer–Tobin _Clough–Kneizys–Davies) [37] continuum model v4.1.1 (latest release version) was used as the continuum for LBLRTM. The MT_CKD model consists of continuum absorption due to $H_2O$, $N_2$, $O_2$, $CO_2$, and $O_3$. In this study, only the $H_2O$ and $CO_2$ continuum were considered for two reasons: (1) $N_2$ and $O_2$ were not included in the simulation; (2) the continuum absorption of $O_3$ is not located in 600–1650 cm$^{-1}$ [61]. The $H_2O$ and $CO_2$ continuum used for ARTS were MT_CKD v3.5.0 and MT_CKD v2.5.2, respectively. The version of MT_CKD used by ARTS is inconsistent with that of LBLRTM because the latest version of MT_CKD is not embedded in ARTS. However, we found no significant change in the $CO_2$ continuum in the selected spectral range by checking the update log. For the $H_2O$ continuum, a non-negligible change is that the temperature-dependence calculation method of the self continuum was changed to a power law in the MT_CKD v3.6. In addition, both ARTS and LBLRTM treat the atmosphere as a set of layers

with equal pressure, and the equivalent pressure of the atmosphere layer is calculated from the pressure of the two boundary levels.

The version of MODTRAN is v5.2.2, and both BM and CK were used for simulation. For BM, the in-band absorption was approximately represented by a statistical expression related to the number of lines and the corresponding line parameters (including the line strength, location, and overlap with other lines) [58]. For CK, the compact tables of k-distributions were generated based on Monte–Carlo methods and 34 ordered k values were contained in each distribution from the minimum to maximum [18,62].

In this study, the simulations were built on a 0.001 $cm^{-1}$ spectral grid for LBLRTM and ARTS and a 0.1 $cm^{-1}$ spectral grid (i.e., the highest spectral resolution for both BM and CK methods) for MODTRAN. Three angles were selected for the simulation, namely 0°, 30°, and 60° off-nadir, and the corresponding incidence angles on the Earth's surface were 0°, 30.4°, and 61.2°. The whole comparison process could be divided into three parts: (1) Comparison on a 0.001 $cm^{-1}$ spectral grid. It should be noted that MODTRAN did not participate in this comparison because of insufficient spectral resolution; (2) the four simulation results (i.e., LBLRTM, ARTS, MODTRAN-BM, and MODTRAN-CK) were convolved with the AIRS spectral response functions to obtain the AIRS channel results before the comparison was performed; and (3) the four simulation results were convolved with the MODIS spectral response functions for comparison on MODIS bands. In this study, a comparison was performed in terms of the brightness temperature. Furthermore, an additional Jacobian comparison was performed for AIRS channels.

### 3.4. Evaluation Criteria

The evaluation criteria of BT included the mean bias difference (MBD) and root mean square difference (RMSD):

$$\begin{aligned} \mathrm{MBD} &= \frac{1}{n}\sum_{i=1}^{n}(y_m - y_r) \\ \mathrm{RMSD} &= \sqrt{\frac{1}{n}\sum_{i=1}^{n}(y_m - y_r)^2} \end{aligned} \tag{6}$$

where $n$ denotes the number of samples, $y_m$ represents the model BT, and $y_r$ represents the reference BT. MBDs and RMSDs were gathered at three levels to analyze the BT difference in detail: (1) The all-grid/channel level, which means gathering the statistic from all grids/channels; (2) the subregion level, which means that the statistics were gathered from all samples in each subregion. Considering the absorption gas type and line strength which differed at different spectra, which could lead the biases between two models to exhibit different characteristics over the spectrum, we divided the 600–1650 $cm^{-1}$ spectral region into six subregions (as shown in Table 3); and (3) the single-grid/channel level, which means statistics were gathered for each grid/channel. In fact, the statistics based at the all-grid/channel level are to obtain the overall difference between the two models; therefore, the explanation is mainly at the subregion level and single-grid/channel level.

**Table 3.** The spectral range and main absorption gases of the six subregions.

| Subregion | Spectral Range ($cm^{-1}$) | Main Absorption Gases |
|---|---|---|
| I | 600–770 | $CO_2$ |
| II | 770–980 | $H_2O$ |
| III | 980–1070 | $O_3$ |
| IV | 1070–1240 | $H_2O$ |
| V | 1240–1360 | $CH_4$, $H_2O$ |
| VI | 1360–1650 | $H_2O$ |

As for the Jacobian comparison, the goodness of fit measure ($M$) was used as evaluation criteria:

$$M = 100\sqrt{\frac{\sum_{i=1}^{N}(J_{m,i} - J_{r,i})^2}{\sum_{i=1}^{N} J_{r,i}{}^2}} \tag{7}$$

where $N$ is the total number of layers; $J_{m,i}$ and $J_{r,i}$ are the model Jacobian and the reference Jacobian at level $i$, respectively. This metric could be used to evaluate the overall accuracy of the model Jacobian rather than on a single layer. The Jacobian calculated by the LBLRTM was used as the reference Jacobian. Generally, $M < 5$ represents the selected model with an excellent fit, and the model with $5 < M < 15$ can be used for NWP applications.

## 4. Results

Here, we present comparison results of the 0.001 cm$^{-1}$ spectral grid, AIRS channels, and MODIS bands. Only Jacobians of different AIRS channels were compared because the selected MODIS bands are insensitive to the atmospheric conditions.

### *4.1. Comparison on 0.001 cm$^{-1}$ Spectral Grid*

The differences in six subregions between ARTS and LBLRTM for all 83 profiles are shown in Figure 2, and the details of the 0.001 cm$^{-1}$ grid can be found in Appendix A. To show the maximum and minimum values of these differences, we used a truncation in Figure 2, and the statistics are shown in Table 4. The difference between the *M-th* percentile and the *N-th* percentile is abbreviated as $D_{\text{M-N}}$ for convenience.

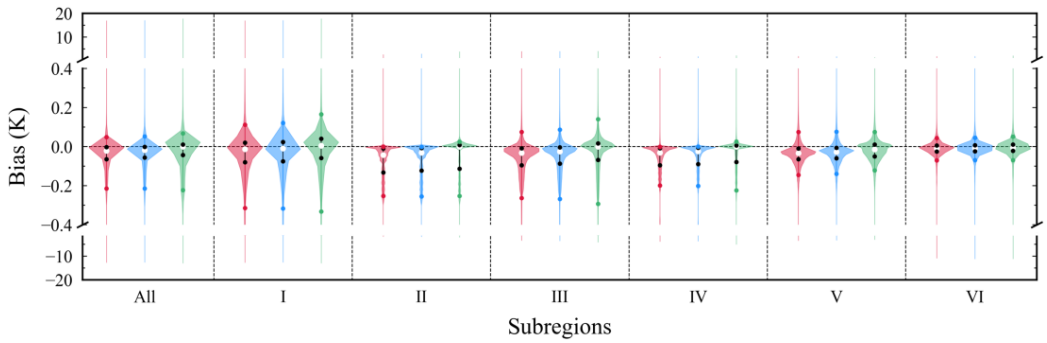


**Figure 2.** The statistics of the differences between ARTS and LBLRTM for all 83 profiles at 0° (the red violin), 30° (the blue violin), and 60° (the green violin). The white dot represents the median, and the two black dots represent the upper and lower quartiles. The two colored dots represent the 5th and 95th percentiles.

It can be seen that more than 90% of the sample differences were distributed within ±0.5 K, and there was a slight systematic underestimation (−0.04 K at 0° and −0.02 K at 60°) at the all-grid level. There were higher differences in subregions I and III, especially in subregion I, than in subregions II, IV, V, and VI. The highest agreement between ARTS and LBLRTM was obtained in subregion VI, and no significant systematic bias was found. In addition, in subregions II and IV, the simulated BT of ARTS was generally lower than that of LBLRTM (more than 95% of the differences were lower than 0 K). These differences in distributions were wider in subregions I, III, and V, accompanied by a slight systematic underestimation.

**Table 4.** The statistics in different percentile intervals. The values outside/inside brackets represent the MBD/RMSD of each subregion, and the unit is K.

| Angle | | All Subregions | Subregion I | Subregion II | Subregion III | Subregion IV | Subregion V | Subregion VI |
|---|---|---|---|---|---|---|---|---|
| 0° | $D_{0–100}$ | −0.04 (0.23) | −0.03 (0.51) | −0.08 (0.12) | −0.05 (0.24) | −0.06 (0.10) | −0.03 (0.09) | −0.01 (0.06) |
| | $D_{0–5}$ | −0.40 (0.66) | −0.86 (1.43) | −0.32 (0.34) | −0.54 (0.61) | −0.28 (0.31) | −0.20 (0.22) | −0.13 (0.17) |
| | $D_{5–95}$ | −0.04 (0.07) | −0.03 (0.09) | −0.07 (0.10) | −0.05 (0.09) | −0.05 (0.08) | −0.04 (0.05) | −0.01 (0.02) |
| | $D_{95–100}$ | 0.27 (0.74) | 0.91 (1.72) | 0.01 (0.03) | 0.56 (0.83) | 0.04 (0.07) | 0.17 (0.21) | 0.10 (0.15) |
| 30° | $D_{0–100}$ | −0.04 (0.24) | −0.02 (0.52) | −0.07 (0.12) | −0.04 (0.25) | −0.06 (0.10) | −0.03 (0.08) | −0.01 (0.06) |
| | $D_{0–5}$ | −0.40 (0.67) | −0.89 (1.48) | −0.33 (0.34) | −0.55 (0.61) | −0.29 (0.32) | −0.20 (0.21) | −0.14 (0.17) |
| | $D_{5–95}$ | −0.03 (0.06) | −0.03 (0.08) | −0.06 (0.10) | −0.05 (0.08) | −0.05 (0.07) | −0.03 (0.05) | −0.01 (0.02) |
| | $D_{95–100}$ | 0.29 (0.76) | 0.96 (1.77) | 0.01 (0.04) | 0.60 (0.86) | 0.05 (0.08) | 0.17 (0.22) | 0.10 (0.15) |
| 60° | $D_{0–100}$ | −0.02 (0.26) | −0.01 (0.58) | −0.05 (0.12) | −0.02 (0.27) | −0.04 (0.11) | −0.02 (0.08) | −0.01 (0.06) |
| | $D_{0–5}$ | −0.43 (0.74) | −1.02 (1.66) | −0.32 (0.34) | −0.57 (0.64) | −0.33 (0.37) | −0.17 (0.19) | −0.14 (0.18) |
| | $D_{5–95}$ | −0.02 (0.06) | −0.01 (0.09) | −0.04 (0.09) | −0.03 (0.09) | −0.04 (0.07) | −0.02 (0.04) | −0.01 (0.02) |
| | $D_{95–100}$ | 0.35 (0.85) | 1.16 (1.96) | 0.04 (0.07) | 0.74 (0.97) | 0.09 (0.13) | 0.18 (0.23) | 0.12 (0.17) |

In subregion I and III, the absolute values of $D_{95–100}$ and $D_{0–5}$ were significantly larger than those of $D_{5–95}$. In subregion I, the means of $D_{95–100}$ ($D_{0–5}$) were 0.91 to 1.16 K (−1.02 to −0.86 K), and the corresponding RMSDs were 1.72 to 1.96 K (1.43 to 1.66 K). To explore the reason, the results of a single gas were also simulated (see Appendix B). The spectral range of subregion I is 600–770 $cm^{-1}$, and the main absorbing gases include $CO_2$, $O_3$, and $H_2O$. The differences in simulated BT (profile 83 and angle 0°) between ARTS and LBLRTM for all gases and three single gases ($CO_2$, $O_3$, and $H_2O$) are shown in Figure 3. It can be seen that most of the points were concentrated near the 0 K line, and only a few points were relatively discrete. Apparently, the differences in the all-gases result were similar to those of $CO_2$ (both the spectral range and magnitude of the difference), and the contribution of $O_3$ and $H_2O$ to differences of BT were much smaller than those of $CO_2$. The reason for this phenomenon is that the strengths of $CO_2$ absorption lines are much greater than those of the other two gases. As for the single-gas results, the number of discrete points of $CO_2$ and $O_3$ is larger than those of $H_2O$ since there are more absorption lines of $CO_2$ and $O_3$ in this subregion than those of $H_2O$. For subregion III (see Figure 4), the deviations were smaller than that of subregion I: the means of $D_{95–100}$ ($D_{0–5}$) are 0.56 to 0.74 K (−0.54 to −0.57 K), and the corresponding RMSDs were 0.83 to 0.97 K (0.61 to 0.64 K). The main absorbing gases in subregion III are the same as in subregion I. However, the contribution of $O_3$ was the largest for the same reason as in subregion I ($O_3$ has the largest number and strength of absorption lines). The wider distribution of BT for subregion V was caused by $CH_4$ absorption lines in this subregion (see Figure A2f-V in Appendix B).

In addition, we found that in some subregions (especially in subregions II, III, and IV), the difference in the version of the $H_2O$ continuum led to lower ARTS single-gas BT simulation results. Taking subregion II as an example (see Figure A2c-II,d-II in Appendix B), when only the absorption lines were considered, the simulated BT difference did not show any systematic underestimation. However, when the continuum was introduced, systematic underestimation occurred. The reason for this is that the $H_2O$ continuum used by the LBLRTM changes the calculation method of temperature dependence to a power law, which is also the reason for the slight systematic underestimation at the all-grid level. However, the order of the systematic underestimation was 0.1 K and could become smaller when other absorption gases (e.g., $CO_2$ and $O_3$) are introduced. For $CO_2$, whether or not the continuum is considered has no significant impact on the distribution of BT differences (see Figure A2a-I–b-I).

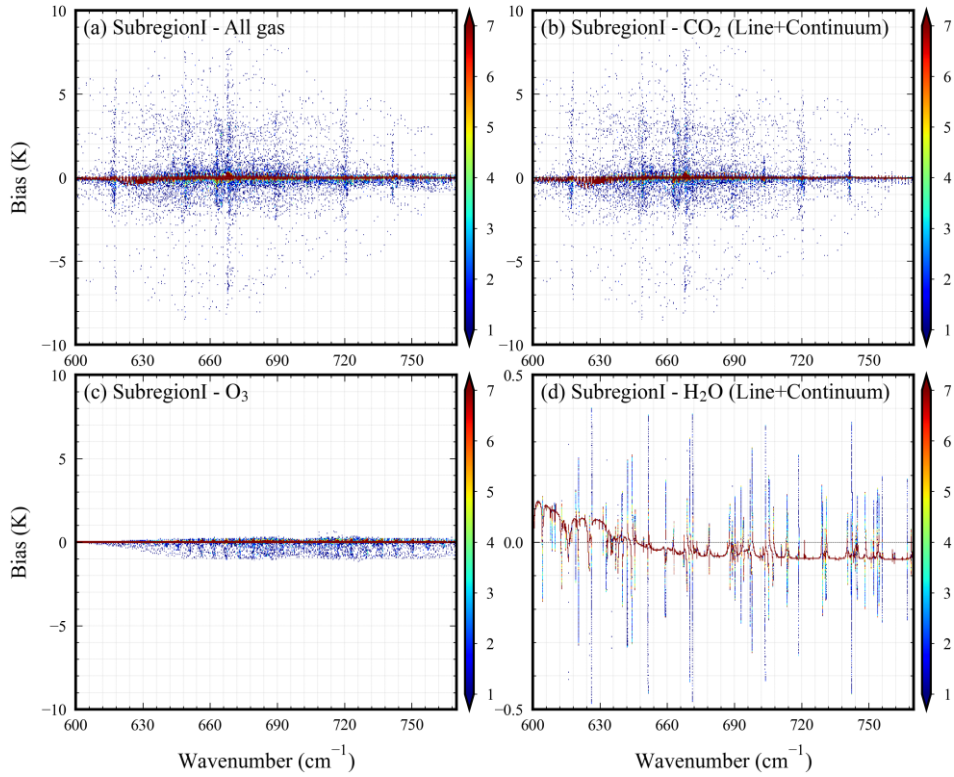


**Figure 3.** The differences between ARTS and LBLRTM for (**a**) all gases, (**b**) $CO_2$ (absorption lines and continuum), (**c**) $O_3$, and (**d**) $H_2O$ (absorption lines and continuum) for profile 83. The color represents the points number in the area: the redder the color, the larger the number, and the bluer, the smaller.

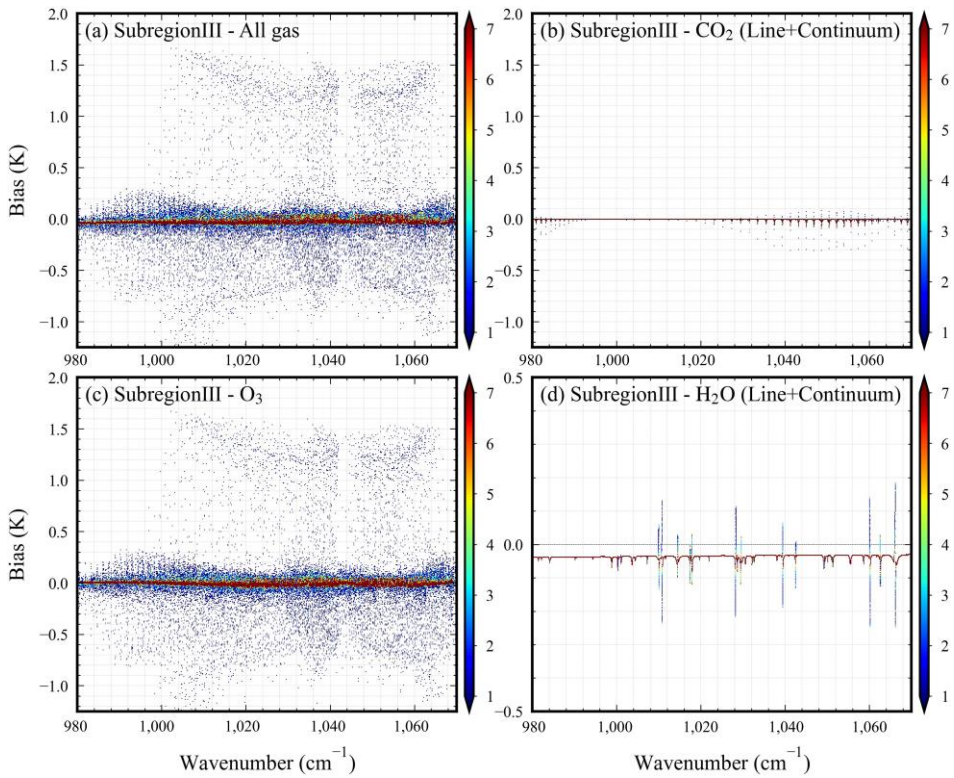


**Figure 4.** As in Figure 3 for subregion III.

### 4.2. Comparison of AIRS Channels

Comparisons were also made between the three RTMs (ARTS, MODTRAN-BM, and MODTRAN-CK) and LBLRTM, after convolving with the AIRS spectral response functions. The corresponding results are shown in Figure 5. As expected, the MBDs and RMSDs of ARTS on AIRS channels were smaller than those on the 0.001 $cm^{-1}$ spectral grid. It can be seen that the discrete points mentioned in Section 4.1 disappeared, and the systematic biases persisted after convolution with AIRS spectral response functions. For example, the underestimations caused by $H_2O$ absorption in Figure 4d in subregion III still exist in Figure 5. At the all-channel level, the BT differences between ARTS and LBLRTM were less than 0.05 K, with a maximum RMSD of 0.08 K for all three angles. In fact, the off-nadir angle did not significantly affect the overall MBD and RMSD (both less than 0.01 K). There was no apparent systematic deviation in subregion I ($CO_2$ is the main absorption gas). Additionally, influenced by the distribution of $CO_2$ absorption lines, the inner systematic deviation line appeared to decrease with the increase in wavenumber. In subregions II, III, and IV, there were systematic underestimations of 0.04–0.07 K, which were caused by the different continuums used by ARTS and LBLRTM (see Section 4.1), and the corresponding RMSE was 0.08–0.12 K. In addition, there exist $O_3$ absorption lines in subregion III, which buffered the systematic underestimation caused by the $H_2O$ continuum, resulting in a smaller underestimation than that in subregions II and IV. In subregions V and VI, there were negligible systematic underestimations: the absolute values of the MBDs were less than 0.03 K, and the corresponding RMSDs were less than 0.05 K. At the single-channel level, the largest MBD (0.17 K) was found at 667.53 $cm^{-1}$ in subregion I, where strong $CO_2$ absorption lines exist nearby, and the largest RMSD was 0.19 K (also found at 667.53 $cm^{-1}$).

The differences between MODTRAN and LBLRTM were much more significant than those of ARTS. At the all-channel level, the MBDs ranged from 0.20 to 0.23 K, the RMSDs ranged from 0.59 to 0.63 K for MODTRAN-BM, and the corresponding MBDs and RMSDs for MODTRAN-CK were from 0.27 to 0.28 K and 0.62 to 0.69 K for the three angles. At the subregion level, it was easy to find apparent systematic overestimation in subregions I and III, with MBDs of ~0.40 K and ~0.9 K. The overestimation of MODTRAN in subregions I and III was due to the absorption of $CO_2$ and $O_3$, respectively: this is a phenomenon that has also been mentioned in previous studies [63]. The differences in other subregions were significantly smaller than in subregion I and III, with a maximum RMSD of 0.56 K. In addition, MODTRAN-BM and MODTRAN-CK performed differently in six subregions: MODTRAN-CK was closer to LBLRTM in subregion I, MODTRAN-BM was closer in subregions II, III, IV, and V, and they were similar in subregion VI. To further give more insight into the atmospheric conditions leading to larger differences, we showed the atmospheric profiles corresponding to RMSDs at the 0/25/50/75/100-th percentile (0-th and 100-th percentile represents the smallest and biggest RMSD, respectively) for different subregions (see Figure 6). Note that only the atmospheric temperature and the most dominant absorbing gas profiles in the subregions were shown. For subregion I, III, and V, RMSD is proportional to atmospheric temperature and the corresponding gas content. For subregion II, IV, and VI, the main absorbing gases are all $H_2O$. However, $H_2O$ continuum dominates in subregions II and IV, and therefore higher atmospheric temperatures and water vapor content lead to larger biases. As for subregion VI, water vapor absorption lines dominate. Since the difference between ARTS and LBLRTM due to water vapor absorption lines is small, the difference does not show a significant positive relationship with atmospheric temperature and water vapor content.

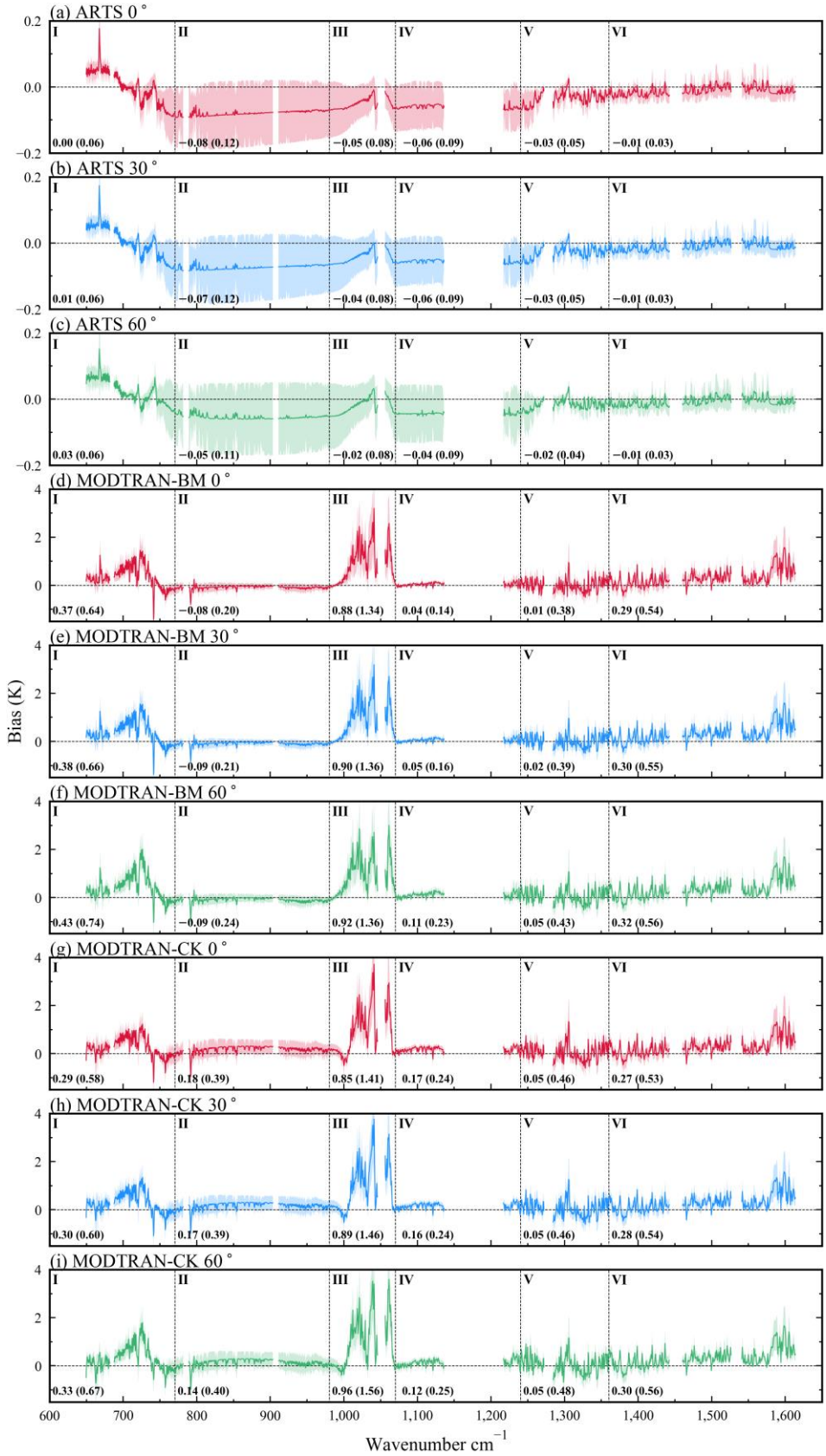


**Figure 5.** BT differences between (**a**–**c**) ARTS, (**d**–**f**) MODTRAN-BM, and (**g**–**i**) MODTRAN-CK and LBLRTM on AIRS channels. The values outside/inside brackets represent the MBD/RMSD of each subregion, and the unit is K.

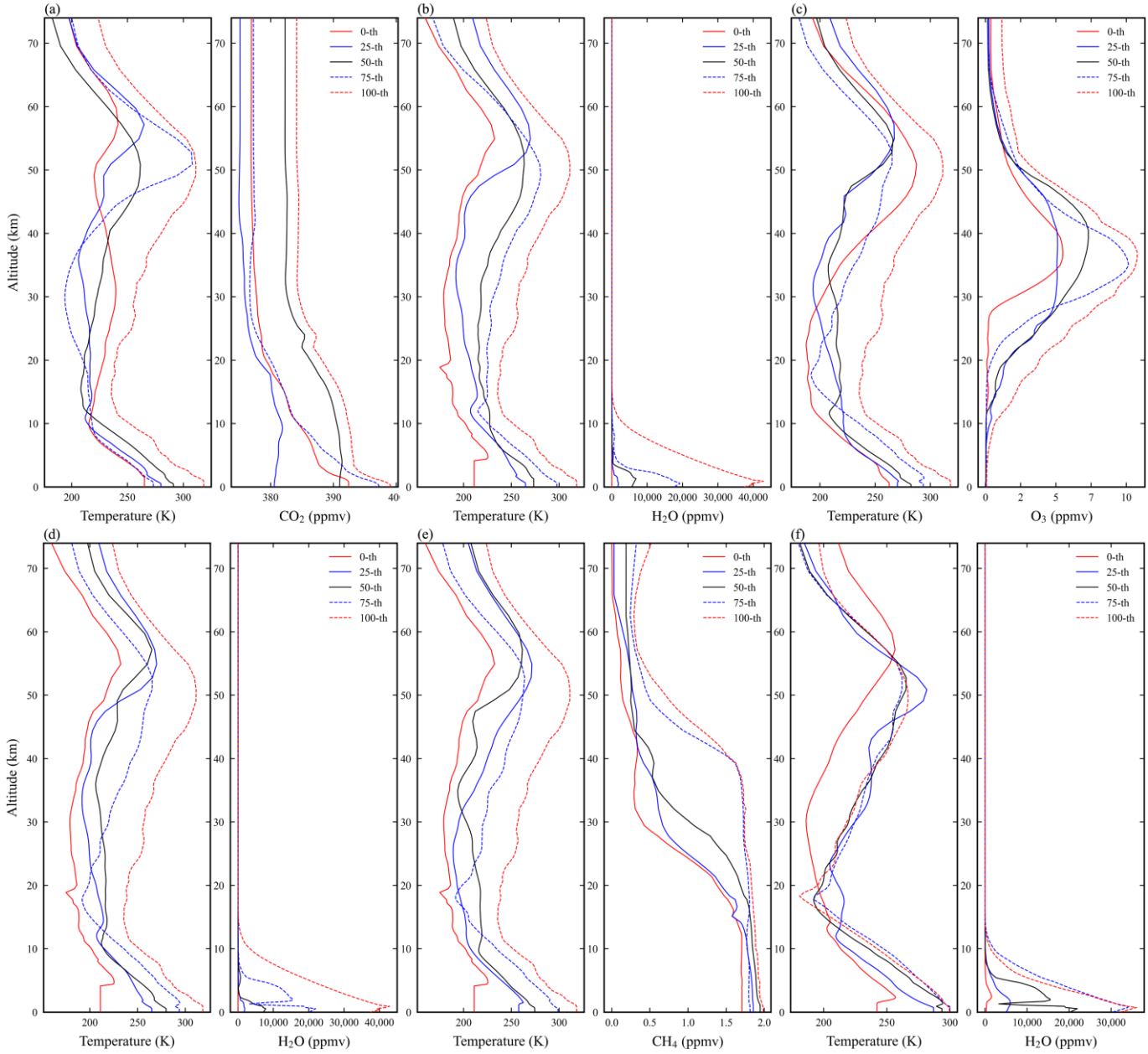


**Figure 6.** The atmospheric profiles corresponding to RMSDs at the 0/25/50/75/100-th percentile for (**a**) Subregion I, (**b**) Subregion II, (**c**) Subregion III, (**d**) Subregion IV, (**e**) Subregion V, (**f**) Subregion VI. The 0-th and 100-th percentile represents the smallest and biggest RMSD, respectively.

In this study, the Jacobians (including temperature, ozone, and water vapor Jacobians) of LBLRTM and ARTS were calculated using the analytical method. In Figure 7, we show the *M* values of profile 81 to 83 at 0° for the temperature Jacobian in subregion I, the ozone Jacobian in subregion III, the water vapor Jacobian in subregion V, and the channel (i.e., channel 243, 999, and 1405) Jacobians corresponding to the maximum *M* value in the three subregions. For the temperature Jacobian, all M values were below 12, and over 50% were below 5. On channel 243, the Jacobians calculated by the LBLRTM and ARTS experienced similar changes in their vertical structure, but the Jacobian of ARTS was higher than that of LBLRTM at 50–600 hPa. For the ozone Jacobian, the two models were incredibly close (*M* values are all below 5). For the water vapor Jacobian, few *M* values were less than 5, indicating a non-negligible difference between the Jacobian calculated by ARTS and LBLRTM. On channel 1405, the most significant difference appeared in

profile 82, and the smallest difference appeared in profile 81, which indicated that the more significant Jacobian difference occurred in the humid atmosphere. However, we found an abnormal phenomenon, i.e., a huge difference in the water vapor Jacobian between ARTS and LBLRTM in the 88–300 hPa of profile 81. After investigation and analysis, we found that the reason for this was the extremely low value (0.016 ppmv) of the volume mixing ratio of water vapor in the 88–300 hPa. From the variation in vertical structure, the water vapor Jacobian calculated by ARTS was more physical than that of LBLRTM, and abnormal mutations appeared in the LBLRTM water vapor Jacobian.

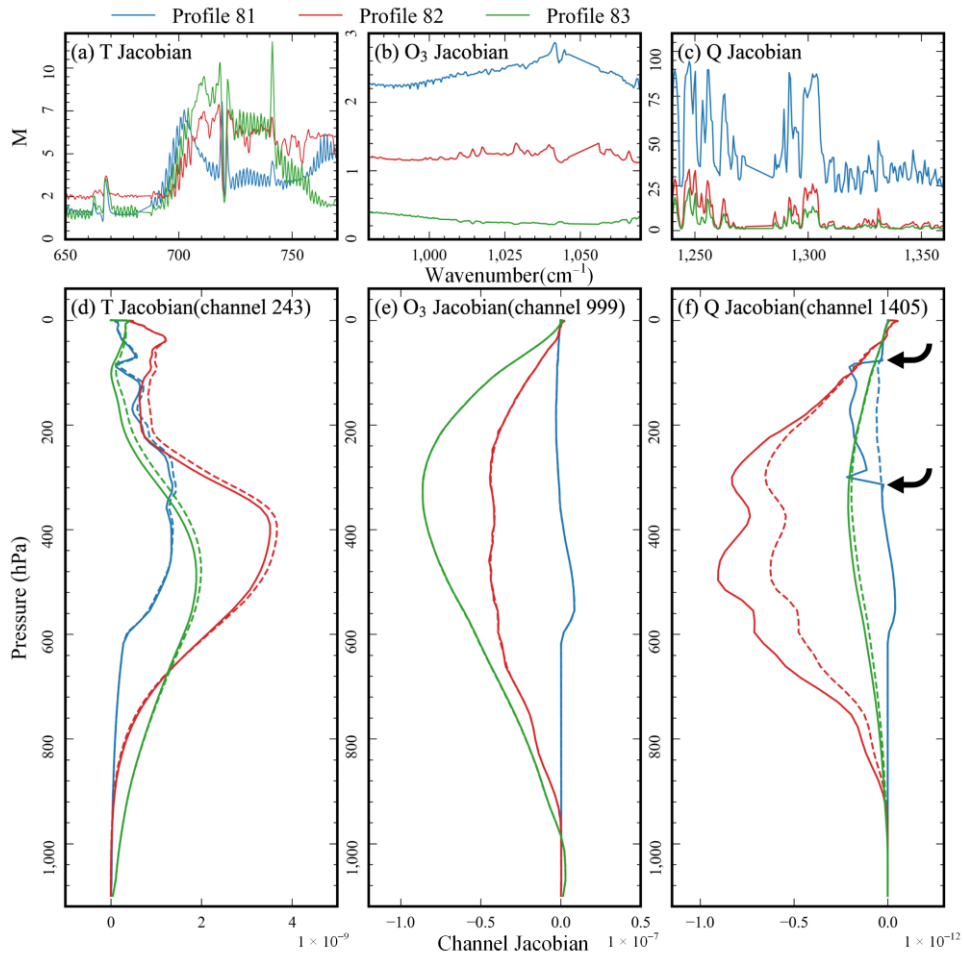


**Figure 7.** The goodness-of-fit measure *M* for (**a**) temperature Jacobian in subregion I, (**b**) ozone Jacobian in subregion III, (**c**) water vapor Jacobian in subregion V, and (**d**–**f**) channel Jacobians corresponding to the maximum *M* value in the three subregions. For (**d**–**f**), the solid and dashed lines represent the channel Jacobians of LBLRTM and ARTS, respectively.

### *4.3. Comparison of MODIS Bands*

For an assessment of the MODIS channels, the simulated results of the four RTMs were convolved with the MODIS spectral response functions to obtain the corresponding BTs of the MODIS channels, and the results are shown in Figure 8. It is easy to conclude that ARTS had the highest agreement with LBLRTM compared to MODTRAN-BM and MODTRAN-CK. At the all-channel level, the MBDs of ARTS ranged from −0.04 to −0.02 K at three angles, with RMSDs of 0.07 K. The corresponding MBDs of MODTRAN-BM were 0.37 to 0.44 K, and RMSDs were 0.69 to 0.74K. The corresponding values of MODTRAN-CK were 0.40 to 0.47 K and 0.66 to 0.74 K.

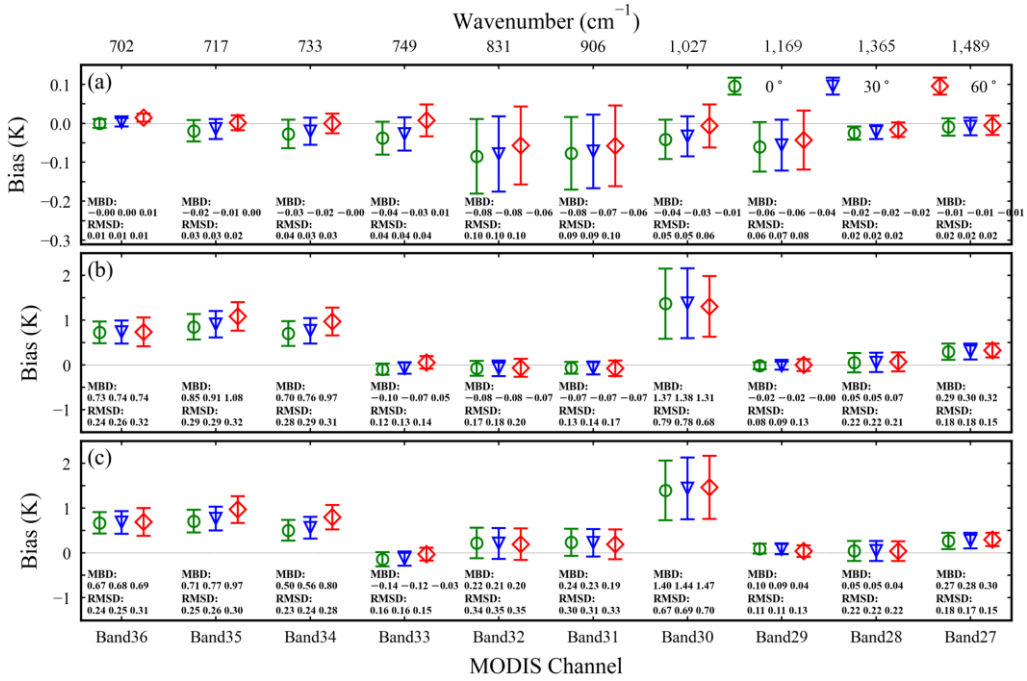


**Figure 8.** BT differences between (**a**) ARTS, (**b**) MODTRAN-BM, and (**c**) MODTRAN-CK and LBLRTM on MODIS bands. The bottom and top axes represent MODIS band numbers and corresponding wavenumbers, respectively.

At the single-channel level, the most significant system underestimation of ARTS occurred in bands 31 and 32 (used to detect surface/cloud temperature), which were mainly affected by the $H_2O$ continuum. The MBDs of bands 31 and 32 ranged from −0.08 to −0.06 K for the three angles, and the corresponding RMSDs were 0.12 to 0.13 K. The MBDs between MODTRAN-BM and LBLRTM in these two channels were close to those of ARTS, but RMSDs were slightly higher (−0.08 K for MBDs and 0.2 K for RMSDs). As for MODTRAN-CK, the differences in MODTRAN-CK for the bands 31 and 32 were more significant than that of the above two models, with MBDs of 0.19 to 0.24 K and RMSDs of 0.38 to 0.41 K. Band 29 is another band that was mainly affected by the $H_2O$ continuum and was used to detect the cloud properties, with a minimal difference between the three RTMs. Bands 33–36 were used to calculate the cloud top altitude, and the main absorbing gas in these four bands was $CO_2$. The ARTS difference in these four bands was slight, reaching 0.01 K for MBDs and 0.01 to 0.02 K for RMSDs in band 36. The difference increased slightly with an increasing wavenumber due to the increasing effect of the $H_2O$ continuum. In band 33, the MBDs ranged from −0.04 to 0.01 K, with RMSDs of 0.04 to 0.06K. In band 30, whose primary use was to detect $O_3$, the most significant system overestimations of MODTRAN-BM and MODTRAN-CK occurred, with MBDs from 1.31 to 1.40 K for MODTRAN-BM and 1.40 to 1.47 K for MODTRAN-CK, and the corresponding RMSDs reaching 1.47 to 1.58 K and 1.55 to 1.63 K. At the same time, ARTS had good consistency with LBLRTM, having MBDs of −0.01 to 0.04 K and RMSDs of 0.06 to 0.07 K. The primary use of bands 27 and 28 was to detect cirrus cloud and water vapor, with ARTS's MBDs ranging from −0.01 to −0.02 K and RMSDs from 0.02 to 0.03 K. The performance of MODTRAN-BM and MODTRAN-CK in bands 27 and 28 was quite different. In band 27, the MBDs were about 0.06 K, and the RMSDs were about 0.23 K. However, in band 28, MBDs exceeded 0.3 K, and RMSDs exceeded 0.34 K.

In summary: (1) regardless of the all-channel or single-channel results, ARTS performs better than MODTRAN-BM and MODTRAN-CK, especially in the spectra where line absorption dominated (e.g., bands 30, 34, 35, and 36). In the spectra where the $H_2O$ continuum dominated (e.g., bands 29, 31, and 32), the MBD values of ARTS were similar to those of MODTRAN-BM. However, the RMSD values of ARTS were much lower, meaning

that ARTS and MODTRAN-BM had a similar systematic deviation, but ARTS was closer to LBLRTM; (2) taking the NEΔT of each MODIS channel as a reference, the ARTS RMSDs were lower than NEΔT for most channels, except for bands 31 and 32, which were used for temperature retrieval with NEΔT of 0.05 K. The ARTS RMSDs exceeded the value of NEΔT by about 0.06 K. MODTRAN-BM and MODTRAN-CK were much larger than the NEΔT values in most channels (except bands 28, 29, and 33), especially in band 30 (the $O_3$ detection band) with an RMSD over 1.5 K.

## 5. Discussion

Line mixing is a phenomenon where the shape of the spectral lines is affected by the closely spaced molecular energy levels [21]. When molecular energy levels change, absorption lines are generated at a specific wavelength/wavenumber/frequency. When the molecular energy levels are closely spaced, many absorption lines are generated in a small spectral range, which results in a change in the shape of the absorption lines. Therefore, the gases with closely spaced molecular energy levels have greater line mixing. Because the absorption lines only generate at a specific wavelength/wavenumber/frequency when the molecular energy levels change, the impact of line mixing occurs mainly in specific spectral ranges. For each individual absorption line, the cross-section can be calculated by [64]

$$\sigma = S(1 - iY + G)F \tag{8}$$

where $\sigma$ is the absorption cross-section; $S$ is the line strength; $i$ is the unit imaginary; $Y$ and $G$ are the first and the second-order line mixing coefficients, respectively; and $F$ is the line shape function. In this study, line mixing was not considered because, currently, ARTS cannot calculate line mixing when the cutoff is turned on. However, line mixing needs to be calculated in practice. Therefore, it is necessary to quantify the "true difference" based on the simulation results of ARTS and LBLRTM (with line mixing). For convenience, the BT difference between ARTS and LBLRTM without/with line mixing was termed $\Delta BT_{NLM}/\Delta BT_{LM}$. Table 5 shows the number of absorption lines separated for each gas and the corresponding number of absorption lines affected by line mixing.

**Table 5.** The number of absorption lines for the simulated five gases and the corresponding number affected by line mixing.

| Gas | Lines | Mixed Lines | Mixed Line Rates |
|---|---|---|---|
| $O_3$ | 121,252 | 0 | 0% |
| $CO_2$ | 113,311 | 84,514 | 74.6% |
| $N_2O$ | 37,195 | 0 | 0% |
| $H_2O$ | 14,583 | 0 | 0% |
| $CH_4$ | 159,377 | 472 | 0.3% |

It is clear that the gases affected by line mixing include $CO_2$ [65,66] and $CH_4$ [67,68]. The ratio of $CO_2$ absorption lines affected by line mixing was 74.6%, while that of $CH_4$ was 0.3%. We found that the line mixing of $CH_4$ caused little difference to the simulation, and this difference was further reduced after convolution with the instrument response (e.g., an order of 0.1 K for the AIRS channel within 1200–1400 $cm^{-1}$). The $\Delta BT_{NLM}$ and $\Delta BT_{LM}$ for profiles 81 to 83 at 0° in subregion I (for $CO_2$) are shown in Figure 9. As mentioned in Section 2.1, profiles 81 and 82 were envelopes of minimum and maximum values, and profile 83 was the mean value. In other words, profile 81 is an extremely cold and dry atmosphere, and profile 82 is an extremely humid and hot atmosphere. It can be found that the wavenumbers affected by $CO_2$ line mixing were mainly distributed around 618, 667, 722, and 742 $cm^{-1}$. At around 618, 722, and 742 $cm^{-1}$, $CO_2$ line mixing led to a higher simulated BT, which caused the $\Delta BT_{LM}$ to appear negative (up to −10 K). However, a contrary phenomenon emerged at around 667 $cm^{-1}$, and $\Delta BT_{LM}$ was below 5 K.

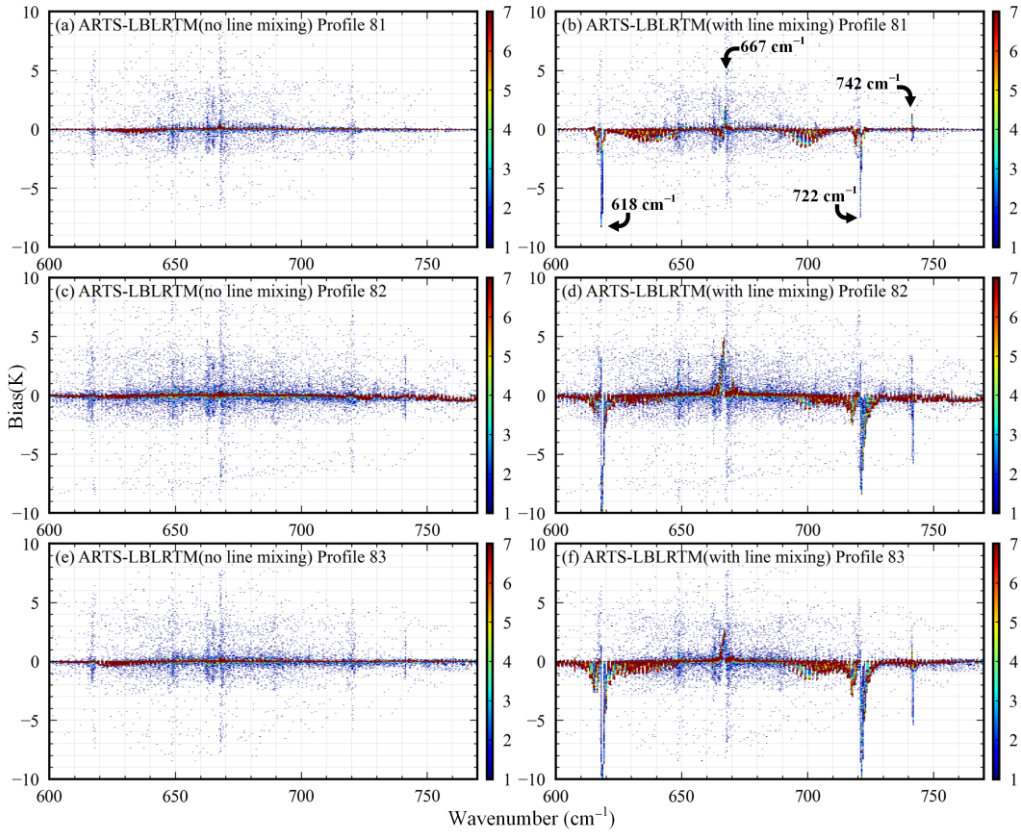


**Figure 9.** The differences between ARTS and LBLRTM (with/no line mixing) for profile (**a**,**b**) 81, (**c**,**d**) 82, and (**e**,**f**) 83 at 0° in subregion I.

After convolving with the AIRS spectral response functions, the $\Delta BT_{LM}$ in different intervals is shown in Table 6. It can be found that in subregion I (600–770 cm$^{-1}$) influenced by $CO_2$ line mixing, the AIRS channel with $\Delta BT_{LM} < 0.2$ K accounted for 51.72%, 33.03%, and 24.65% for profiles 81, 83, and 82, respectively. $\Delta BT_{LM}$ exhibited a positive correlation with atmospheric temperature. However, for the three profiles, the proportions of the AIRS channels with $\Delta BT_{LM} < 0.5$ K were all over 70%. In 600–1650 cm$^{-1}$, the proportions of the AIRS channels with $\Delta BT_{LM} < 0.2$ K showed the same trend as subregion I but with higher values. It can be seen that the $\Delta BT_{LM}$ of profile 82 was larger than that of the other two profiles. The reason is that profile 82 had the highest water vapor and atmospheric temperature and was, therefore, more affected by the version of the $H_2O$ continuum. For profiles 81 and 83, the $\Delta BT_{LM}$ of more than 90% of the AIRS channels was less than 0.5 K.

**Table 6.** The percentages of the BT difference between ARTS and LBLRTM (with line mixing) for profiles 81 to 83 in 600–770 cm$^{-1}$ and 600–1650 cm$^{-1}$.

| Spectral Range | Profile | ARTS-LBLRTM (with Line Mixing) | | | |
|---|---|---|---|---|---|
| | | $\lvert\Delta BT\rvert < 0.2$ K | 0.2 K < $\lvert\Delta BT\rvert < 0.5$ K | 0.5 K < $\lvert\Delta BT\rvert < 1$ K | $\lvert\Delta BT\rvert > 1$ K |
| 600–770 cm$^{-1}$ | 81 | 51.72% | 33.01% | 13.06% | 2.21% |
| | 83 | 33.03% | 37.43% | 21.42% | 8.12% |
| | 82 | 24.65% | 48.27% | 19.45% | 7.63% |
| 600–1650 cm$^{-1}$ | 81 | 89.49% | 7.19% | 2.84% | 0.48% |
| | 83 | 74.19% | 16.41% | 7.63% | 1.77% |
| | 82 | 29.94% | 24.57% | 43.40% | 2.09% |

As for the MODIS bands, line mixing had a negligible effect for bands 27 to 33 (the differences between $\Delta BT_{NLM}$ and $\Delta BT_{LM}$ were less than 0.05 K). The most significant difference between $\Delta BT_{NLM}$ and $\Delta BT_{LM}$ occurred in MODIS band 35 and could achieve

1 K. For bands 34 and 36, $\Delta BT_{NLM}$-$\Delta BT_{LM}$ ranged from 0.06 to 0.48 K and 0.21 to 0.38 K, respectively.

## 6. Conclusions

A comparison study was conducted to investigate the performance of the Atmospheric Radiative Transfer Simulator (ARTS, commonly used in the microwave to terahertz region) in the thermal infrared (TIR) region. The selected reference radiative transfer model (RTM) was the Line-By-Line Radiative Transfer Model (LBLRTM), and the moderate resolution atmospheric transmission (MODTRAN) band model (BM) and correlated-k (CK) methods were also used for comparison. The simulated spectral range was 600–1650 $cm^{-1}$, and three angles were selected in the simulation, namely 0°, 30°, and 60° off-nadir. The comparison process could be divided into three parts: (1) on the 0.001 $cm^{-1}$ spectral grid; (2) on AIRS channels; and (3) on MODIS bands.

The 0.001 $cm^{-1}$ spectral grid comparison results showed a high agreement between ARTS and LBLRTM. In 600–1650 $cm^{-1}$, the mean bias difference (MBD) and root mean square difference (RMSD) were less than 0.05 K and 0.3 K, respectively. Larger differences occurred where the absorption lines were dense and affected by the water vapor continuum. For the former, differences due to absorption lines appeared as discrete points (i.e., no apparent systematic deviation), and this difference was proportional to the line strength of the absorbing line. As for the water vapor continuum, differences were systematic in most cases due to the different versions of the $H_2O$ continuum used by ARTS and LBLRTM.

After convolving with AIRS's spectral response functions, the differences between ARTS and LBLRTM became smaller. The BT differences between ARTS and LBLRTM were less than 0.05 K, with a maximum RMSD of 0.08 K for all three angles. In addition, the maximum channel RMSD occurred at 667.53 $cm^{-1}$, and the value was 0.19 K. However, MODTRAN-BM and MODTRAN-CK exhibited RMSDs of ~0.6 K and performed poorly, where $CO_2$ and $O_3$ absorption was strong (with a maximum channel RMSD of 4 K). The comparison results for the Jacobian show that the goodness of fit measure ($M$) was less than 15 (means can be used for Numerical Weather Prediction application) for the temperature Jacobian and less than 5 for the $O_3$ Jacobian (an excellent Jacobian fit). However, few $M$ values were less than 5 for the water vapor Jacobian, and the maximum $M$ could exceed 100. On the one hand, the difference between the two water vapor Jacobians calculated by ARTS and LBLRTM increased with increasing water vapor content. On the other hand, at extremely low water vapor values (0.016 ppmv in this study), LBLRTM exhibited non-physical mutations. As for the MODIS bands, the MBDs of ARTS ranged from −0.04 to −0.02 K at three angles, with RMSDs of 0.07 K. The MBDs of MODTRAN-BM were 0.37 to 0.44 K, and RMSDs were 0.69 to 0.74K. The corresponding values of MODTRAN-CK were 0.40 to 0.47 K and 0.66 to 0.74 K. The findings of this study aim to help users understand the accuracy of ARTS in the TIR region and the improvement of ARTS via the community.

**Author Contributions:** Conceptualization, Z.J. and Z.L.; Data curation, Y.L.; Formal analysis, Z.J. and S.W.; Funding acquisition, Y.L.; Investigation, Z.J. and S.W.; Methodology, Z.J. and Z.L.; Project administration, Y.L.; Resources, Z.L.; Software, Z.J. and S.W.; Supervision, Z.L. and Y.L.; Validation, Z.J. and S.W.; Visualization, Z.J.; Writing—original draft, Z.J. and S.W.; Writing—review and editing, Z.L. All authors have read and agreed to the published version of the manuscript.

**Funding:** This research was funded by the Shanghai Pilot Program for Basic Research—Chinese Academy of Sciences, Shanghai Branch (grant number: JCYJ-SHFY-2022-004).

**Data Availability Statement:** Data available on request from the authors.

**Acknowledgments:** The authors would like to thank Universität Hamburg and Chalmers University for providing ARTS (https://www.radiativetransfer.org/, accessed on 15 July 2023) and Atmospheric and Environmental Research R&C (AER-RC) for providing LBLRTM (https://www.aer.com/science-research/atmosphere/radiative-transfer/, accessed on 15 July 2023). We also thank EUMETSAT Numerical Weather Prediction Satellite Application Facility (NWP SAF) for providing the 101-level profiles.

**Conflicts of Interest:** The authors declare no conflict of interest.

## Appendix A

The BT difference between ARTS and LBLRTM (no line mixing) on 0.001 $cm^{-1}$ spectral grid is illustrated in Figure A1.

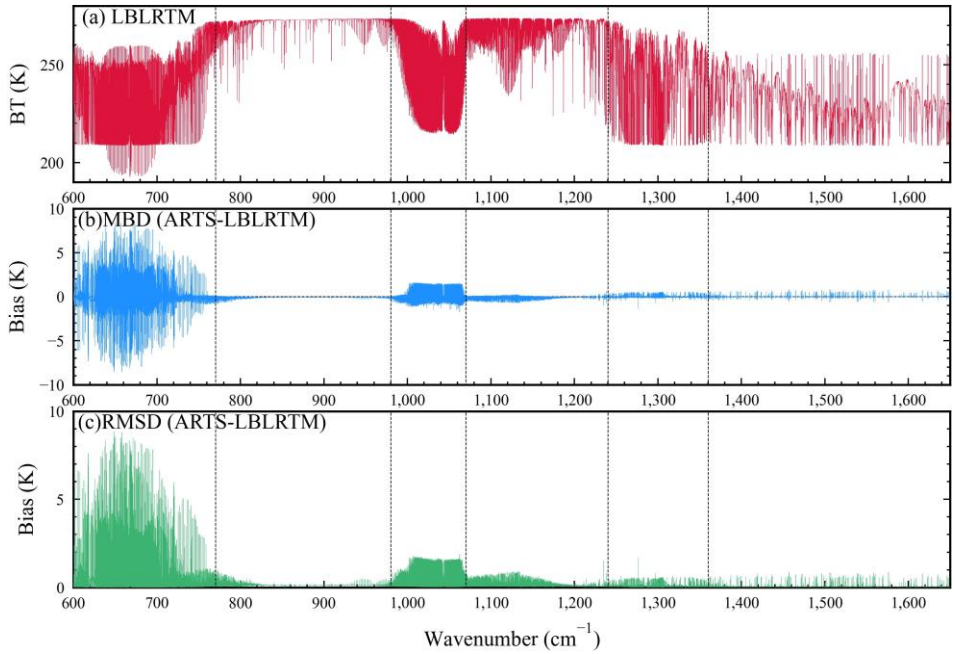


**Figure A1.** BT consistency between ARTS and LBLRTM as a function of wavenumber: (**a**) BTs simulated by LBLRTM for profile 83; (**b**) MBDs and (**c**) RMSDs of the BT differences for all 83 profiles.

## Appendix B

The differences of the simulated BT (profile 83 and angle 0°) between ARTS and LBLRTM for the selected five single gases ($CO_2$, $O_3$, $H_2O$, $CH_4$, and $N_2O$) are highlighted in Figure A2. For $CO_2$ and $H_2O$, the continuums were not simulated separately but together with the corresponding absorption lines.

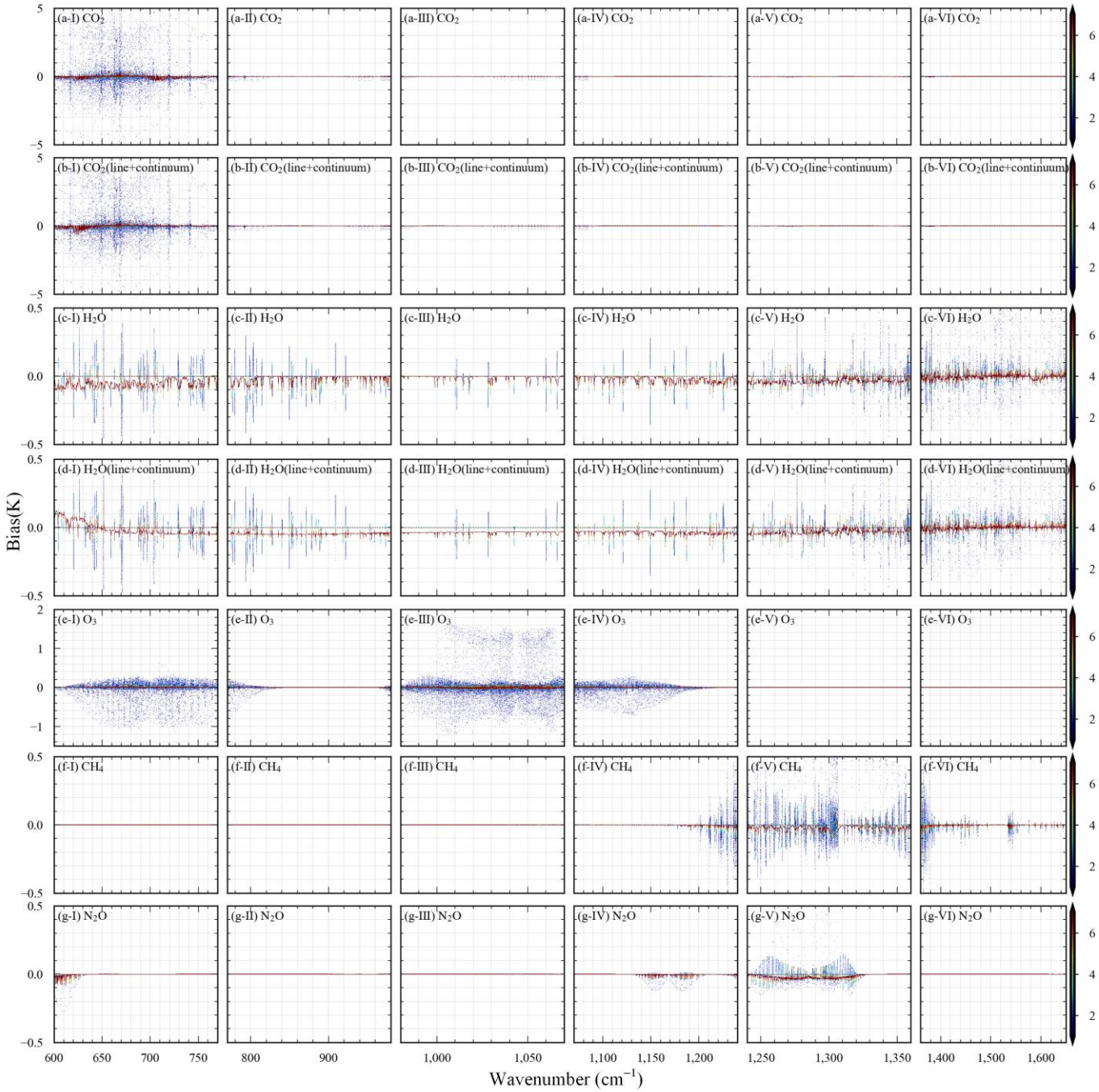


**Figure A2.** BT consistency (profile 83 and 0°) between ARTS and LBLRTM as a function of wavenumber for the five single gases, i.e., (**a**,**b**) $CO_2$, (**c**,**d**) $H_2O$, (**e**) $O_3$, (**f**) $CH_4$, and (**g**) $N_2O$. (**I**–**VI**) represent different subregions.

## References


1. Vogelmann, J.E.; Helder, D.; Morfitt, R.; Choate, M.J.; Merchant, J.W.; Bulley, H. Effects of Landsat 5 Thematic Mapper and Landsat 7 Enhanced Thematic Mapper Plus Radiometric and Geometric Calibrations and Corrections on Landscape Characterization. *Remote Sens. Environ.* **2001**, *78*, 55–70. [CrossRef]
2. Chapman, J.W.; Thompson, D.R.; Helmlinger, M.C.; Bue, B.D.; Green, R.O.; Eastwood, M.L.; Geier, S.; Olson-Duvall, W.; Lundeen, S.R. Spectral and Radiometric Calibration of the next Generation Airborne Visible Infrared Spectrometer (AVIRIS-NG). *Remote Sens.* **2019**, *11*, 2129. [CrossRef]
3. Tang, H.; Xie, J.; Tang, X.; Chen, W.; Li, Q. On-Orbit Radiometric Performance of GF-7 Satellite Multispectral Imagery. *Remote Sens.* **2022**, *14*, 886. [CrossRef]

4. Li, J.; Wolf, W.W.; Menzel, W.P.; Zhang, W.; Huang, H.-L.; Achtor, T.H. Global Soundings of the Atmosphere from ATOVS Measurements: The Algorithm and Validation. *J. Appl. Meteorol. Climatol.* **2000**, *39*, 1248–1268. [CrossRef]
5. Eyre, J.; Kelly, G.; McNally, A.; Andersson, E.; Persson, A. Assimilation of TOVS Radiance Information through One-Dimensional Variational Analysis. *Q. J. R. Meteorol. Soc.* **1993**, *119*, 1427–1463. [CrossRef]
6. Moradi, I.; Goldberg, M.; Brath, M.; Ferraro, R.; Buehler, S.A.; Saunders, R.; Sun, N. Performance of Radiative Transfer Models in the Microwave Region. *J. Geophys. Res. Atmos.* **2020**, *125*, e2019JD031831. [CrossRef]
7. Rothman, L.S.; Gordon, I.E.; Babikov, Y.; Barbe, A.; Benner, D.C.; Bernath, P.F.; Birk, M.; Bizzocchi, L.; Boudon, V.; Brown, L.R.; et al. The HITRAN2012 Molecular Spectroscopic Database. *J. Quant. Spectrosc. Radiat. Transf.* **2013**, *130*, 4–50. [CrossRef]
8. Gordon, I.E.; Rothman, L.S.; Hill, C.; Kochanov, R.V.; Tan, Y.; Bernath, P.F.; Birk, M.; Boudon, V.; Campargue, A.; Chance, K.; et al. The HITRAN2016 Molecular Spectroscopic Database. *J. Quant. Spectrosc. Radiat. Transf.* **2017**, *203*, 3–69.
9. Rothman, L.S. History of the HITRAN Database. *Nat. Rev. Phys.* **2021**, *3*, 302–304. [CrossRef]
10. Clough, S.A.; Iacono, M.J.; Moncet, J.-L. Line-by-Line Calculations of Atmospheric Fluxes and Cooling Rates: Application to Water Vapor. *J. Geophys. Res. Atmos.* **1992**, *97*, 15761–15785. [CrossRef]
11. Berk, A.; Anderson, G.P.; Acharya, P.K.; Bernstein, L.S.; Muratov, L.; Lee, J.; Fox, M.; Adler-Golden, S.M.; Chetwynd, J.H.; Hoke, M.L.; et al. MODTRAN 5: A Reformulated Atmospheric Band Model with Auxiliary Species and Practical Multiple Scattering Options: Update. In Proceedings of the Algorithms and Technologies for Multispectral, Hyperspectral, and Ultraspectral Imagery XI, Orlando, FL, USA, 28 March–1 April 2005; SPIE: Washington, DC, USA, 2005; Volume 5806, pp. 662–667.
12. Goody, R.; West, R.; Chen, L.; Crisp, D. The Correlated-k Method for Radiation Calculations in Nonhomogeneous Atmospheres. *J. Quant. Spectrosc. Radiat. Transf.* **1989**, *42*, 539–550. [CrossRef]
13. Pierluissi, J.H.; Peng, G.-S. New Molecular Transmission Band Models for LOWTRAN. *Opt. Eng.* **1985**, *24*, 541–547. [CrossRef]
14. Vincent, R.A.; Dudhia, A. Fast Radiative Transfer Using Monochromatic Look-up Tables. *J. Quant. Spectrosc. Radiat. Transf.* **2017**, *186*, 254–264. [CrossRef]
15. Andersson, E.; Haseler, J.; Undén, P.; Courtier, P.; Kelly, G.; Vasiljevic, D.; Brankovic, C.; Gaffard, C.; Hollingsworth, A.; Jakob, C.; et al. The ECMWF Implementation of Three-Dimensional Variational Assimilation (3D-Var). III: Experimental Results. *Q. J. R. Meteorol. Soc.* **1998**, *124*, 1831–1860.
16. Saunders, R.; Hocking, J.; Turner, E.; Rayer, P.; Rundle, D.; Brunel, P.; Vidot, J.; Roquet, P.; Matricardi, M.; Geer, A.; et al. An Update on the RTTOV Fast Radiative Transfer Model (Currently at Version 12). *Geosci. Model Dev.* **2018**, *11*, 2717–2737. [CrossRef]
17. Weng, F.; Yu, X.; Duan, Y.; Yang, J.; Wang, J. Advanced Radiative Transfer Modeling System (ARMS): A New-Generation Satellite Observation Operator Developed for Numerical Weather Prediction and Remote Sensing Applications. *Adv. Atmos. Sci.* **2020**, *37*, 131–136. [CrossRef]
18. Berk, A.; Hawes, F. Validation of MODTRAN®6 and Its Line-by-Line Algorithm. *J. Quant. Spectrosc. Radiat. Transf.* **2017**, *203*, 542–556. [CrossRef]
19. Berk, A.; Conforti, P.; Hawes, F. An Accelerated Line-by-Line Option for MODTRAN Combining on-the-Fly Generation of Line Center Absorption within 0.1 $cm^{-1}$ Bins and Pre-Computed Line Tails. In Proceedings of the Algorithms and Technologies for Multispectral, Hyperspectral, and Ultraspectral Imagery XXI, Baltimore, MD, USA, 21 May 2015; SPIE: Washington, DC, USA, 2015; Volume 9472, pp. 405–415.
20. Buehler, S.A.; Eriksson, P.; Kuhn, T.; von Engeln, A.; Verdes, C. ARTS, the Atmospheric Radiative Transfer Simulator. *J. Quant. Spectrosc. Radiat. Transf.* **2005**, *91*, 65–93. [CrossRef]
21. Buehler, S.A.; Mendrok, J.; Eriksson, P.; Perrin, A.; Larsson, R.; Lemke, O. ARTS, the Atmospheric Radiative Transfer Simulator-Version 2.2, the Planetary Toolbox Edition. *Geosci. Model Dev.* **2018**, *11*, 1537–1556. [CrossRef]
22. Eriksson, P.; Buehler, S.A.; Davis, C.P.; Emde, C.; Lemke, O. ARTS, the Atmospheric Radiative Transfer Simulator, Version 2. *J. Quant. Spectrosc. Radiat. Transf.* **2011**, *112*, 1551–1558. [CrossRef]
23. Eriksson, P.; Rydberg, B.; Mattioli, V.; Thoss, A.; Accadia, C.; Klein, U.; Buehler, S.A. Towards an Operational Ice Cloud Imager (ICI) Retrieval Product. *Atmos. Meas. Tech.* **2020**, *13*, 53–71. [CrossRef]
24. Bobryshev, O.; Buehler, S.A.; John, V.O.; Brath, M.; Brogniez, H. Is There Really a Closure Gap between 183.31-GHz Satellite Passive Microwave and in Situ Radiosonde Water Vapor Measurements? *IEEE Trans. Geosci. Remote Sens.* **2018**, *56*, 2904–2910. [CrossRef]
25. Barlakas, V.; Galligani, V.S.; Geer, A.J.; Eriksson, P. On the Accuracy of RTTOV-SCATT for Radiative Transfer at All-Sky Microwave and Submillimeter Frequencies. *J. Quant. Spectrosc. Radiat. Transf.* **2022**, *283*, 108137. [CrossRef]
26. Buehler, S.; Von Engeln, A.; Brocard, E.; John, V.O.; Kuhn, T.; Eriksson, P. Recent Developments in the Line-by-Line Modeling of Outgoing Longwave Radiation. *J. Quant. Spectrosc. Radiat. Transf.* **2006**, *98*, 446–457. [CrossRef]
27. John, V.O.; Buehler, S.; von Engeln, A.; Eriksson, P.; Kuhn, T.; Brocard, E.; Koenig-langlo, G. Understanding the Variability of Clear-Sky Outgoing Long-Wave Radiation Based on Ship-Based Temperature and Water Vapour Measurements. *Q. J. R. Meteorol. Soc. A J. Atmos. Sci. Appl. Meteorol. Phys. Oceanogr.* **2006**, *132*, 2675–2691. [CrossRef]
28. Melsheimer, C.; Verdes, C.; Buehler, S.A.; Emde, C.; Eriksson, P.; Feist, D.G.; Ichizawa, S.; John, V.O.; Kasai, Y.; Kopp, G.; et al. Intercomparison of General Purpose Clear Sky Atmospheric Radiative Transfer Models for the Millimeter/Submillimeter Spectral Range. *Radio Sci.* **2005**, *40*, 1–25. [CrossRef]
29. Buehler, S.; Courcoux, N.; John, V.O. Radiative Transfer Calculations for a Passive Microwave Satellite Sensor: Comparing a Fast Model and a Line-by-Line Model. *J. Geophys. Res. Atmos.* **2006**, *111*. [CrossRef]

30. Schreier, F.; Milz, M.; Buehler, S.A.; Von Clarmann, T. Intercomparison of Three Microwave/Infrared High Resolution Line-by-Line Radiative Transfer Codes. *J. Quant. Spectrosc. Radiat. Transf.* **2018**, *211*, 64–77. [CrossRef]
31. Saunders, R.; Rayer, P.; Brunel, P.; Von Engeln, A.; Bormann, N.; Strow, L.; Hannon, S.; Heilliette, S.; Liu, X.; Miskolczi, F.; et al. A Comparison of Radiative Transfer Models for Simulating Atmospheric Infrared Sounder (AIRS) Radiances. *J. Geophys. Res.* **2007**, *112*, D01S90. [CrossRef]
32. Chahine, M.T.; Pagano, T.S.; Aumann, H.H.; Atlas, R.; Barnet, C.; Blaisdell, J.; Chen, L.; Divakarla, M.; Fetzer, E.J.; Goldberg, M.; et al. AIRS: Improving Weather Forecasting and Providing New Data on Greenhouse Gases. *Bull. Am. Meteorol. Soc.* **2006**, *87*, 911–926. [CrossRef]
33. Clough, S.; Shephard, M.; Mlawer, E.; Delamere, J.; Iacono, M.; Cady-Pereira, K.; Boukabara, S.; Brown, P. Atmospheric Radiative Transfer Modeling: A Summary of the AER Codes. *J. Quant. Spectrosc. Radiat. Transf.* **2005**, *91*, 233–244. [CrossRef]
34. Alvarado, M.J.; Payne, V.H.; Mlawer, E.J.; Uymin, G.; Shephard, M.W.; Cady-Pereira, K.E.; Delamere, J.S.; Moncet, J.-L. Performance of the Line-By-Line Radiative Transfer Model (LBLRTM) for Temperature, Water Vapor, and Trace Gas Retrievals: Recent Updates Evaluated with IASI Case Studies. *Atmos. Chem. Phys.* **2013**, *13*, 6687–6711. [CrossRef]
35. Saeed, A.; Gurbuz, O.; Akkas, M.A. Terahertz Communications at Various Atmospheric Altitudes. *Phys. Commun.* **2020**, *41*, 101113. [CrossRef]
36. Zhang, F.; Zhu, M.; Li, J.; Li, W.; Di, D.; Shi, Y.-N.; Wu, K. Alternate Mapping Correlated K-Distribution Method for Infrared Radiative Transfer Forward Simulation. *Remote Sens.* **2019**, *11*, 994. [CrossRef]
37. Mlawer, E.J.; Payne, V.H.; Moncet, J.-L.; Delamere, J.S.; Alvarado, M.J.; Tobin, D.C. Development and Recent Evaluation of the MT_CKD Model of Continuum Absorption. *Philos. Trans. R. Soc. A Math. Phys. Eng. Sci.* **2012**, *370*, 2520–2556. [CrossRef] [PubMed]
38. Delamere, J.; Clough, S.; Payne, V.; Mlawer, E.; Turner, D.; Gamache, R. A Far-Infrared Radiative Closure Study in the Arctic: Application to Water Vapor. *J. Geophys. Res. Atmos.* **2010**, *115*. [CrossRef]
39. Mlawer, E.; Turner, D.; Paine, S.; Palchetti, L.; Bianchini, G.; Payne, V.; Cady-Pereira, K.; Pernak, R.; Alvarado, M.; Gombos, D.; et al. Analysis of Water Vapor Absorption in the Far-Infrared and Submillimeter Regions Using Surface Radiometric Measurements from Extremely Dry Locations. *J. Geophys. Res. Atmos.* **2019**, *124*, 8134–8160. [CrossRef]
40. Amato, U.; Masiello, G.; Serio, C.; Viggiano, M. The σ-IASI Code for the Calculation of Infrared Atmospheric Radiance and Its Derivatives. *Environ. Model. Softw.* **2002**, *17*, 651–667. [CrossRef]
41. Tjemkes, S.A.; Patterson, T.; Rizzi, R.; Shephard, M.W.; Clough, S.A.; Matricardi, M.; Haigh, J.D.; Höpfner, M.; Payan, S.; Trotsenko, A.; et al. The ISSWG Line-by-Line Inter-Comparison Experiment. *J. Quant. Spectrosc. Radiat. Transf.* **2003**, *77*, 433–453. [CrossRef]
42. Pernini, T.; Zaccheo, T.S. Impact of Spectroscopic and Atmospheric State Knowledge on Retrieved $XCO_2$ and $XCH_4$ Column Amounts from Laser Differential Absorption Spectrometer Measurements. In Proceedings of the AGU Fall Meeting Abstracts, New Orleans, LA, USA, 11 December 2017; Volume 2017, pp. 23–2349.
43. Saunders, R.; Hocking, J.; Turner, E.; Havemann, S.; Geer, A.; Lupu, C.; Vidot, J.; Chambon, P.; Köpken-Watts, C.; Scheck, L.; et al. *RTTOV-13 Science and Validation Report, EUMETSAT NWP-SAF*; Met Office: Exeter, UK, 2020.
44. Johnson, B.T.; Dang, C.; Stegmann, P.; Liu, Q.; Moradi, I.; Auligne, T. The Community Radiative Transfer Model (CRTM): Community-Focused Collaborative Model Development Accelerating Research to Operations. *Bull. Am. Meteorol. Soc.* **2023**. [CrossRef]
45. Jiao, Z.-H.; Mu, X. Global Validation of Clear-Sky Models for Retrieving Land-Surface Downward Longwave Radiation from MODIS Data. *Remote Sens. Environ.* **2022**, *271*, 112903. [CrossRef]
46. Li, R.; Li, H.; Hu, T.; Bian, Z.; Liu, F.; Cao, B.; Du, Y.; Sun, L.; Liu, Q. Land Surface Temperature Retrieval From Sentinel-3A SLSTR Data: Comparison Among Split-Window, Dual-Window, Three-Channel, and Dual-Angle Algorithms. *IEEE Trans. Geosci. Remote Sens.* **2023**, *61*, 1–14. [CrossRef]
47. Galve, J.M.; Sánchez, J.M.; García-Santos, V.; González-Piqueras, J.; Calera, A.; Villodre, J. Assessment of Land Surface Temperature Estimates from Landsat 8-TIRS in A High-Contrast Semiarid Agroecosystem. Algorithms Intercomparison. *Remote Sens.* **2022**, *14*, 1843. [CrossRef]
48. Berk, A.; Anderson, G.P.; Acharya, P.K.; Bernstein, L.S.; Muratov, L.; Lee, J.; Fox, M.; Adler-Golden, S.M.; Chetwynd, J.H.; Hoke, M.L.; et al. MODTRAN5: 2006 Update. In Proceedings of the Algorithms and Technologies for Multispectral, Hyperspectral, and Ultraspectral Imagery XII, Kissimmee, FL, USA, 17–20 April 2006; SPIE: Washington, DC, USA, 2006; Volume 6233, pp. 508–515.
49. Matricardi, M. The Generation of RTTOV Regression Coefficients for IASI and AIRS Using a New Profile Training Set and a New Line-by-Line Database. In *ECMWF Technical Memoranda*; ECMWE: Reading, UK, 2008; p. 47.
50. Chevallier, F.; Michele, S.D.; McNally, A. *Diverse Profile Datasets from the ECMWF 91-Level Short-Range Forecasts*; ECMWF: Reading, UK, 2006.
51. Salomonson, V.V.; Barnes, W.; Maymon, P.W.; Montgomery, H.E.; Ostrow, H. MODIS: Advanced Facility Instrument for Studies of the Earth as a System. *IEEE Trans. Geosci. Remote Sens.* **1989**, *27*, 145–153. [CrossRef]
52. Aumann, H.H.; Chahine, M.T.; Gautier, C.; Goldberg, M.D.; Kalnay, E.; McMillin, L.M.; Revercomb, H.; Rosenkranz, P.W.; Smith, W.L.; Staelin, D.H.; et al. AIRS/AMSU/HSB on the Aqua Mission: Design, Science Objectives, Data Products, and Processing Systems. *IEEE Trans. Geosci. Remote Sens.* **2003**, *41*, 253–264. [CrossRef]
53. Buehler, S.A.; Eriksson, P.; Lemke, O. Absorption Lookup Tables in the Radiative Transfer Model ARTS. *J. Quant. Spectrosc. Radiat. Transf.* **2011**, *112*, 1559–1567. [CrossRef]

54. Zhang, C.; Wu, L.; Zheng, C.; Gkioulekas, I.; Ramamoorthi, R.; Zhao, S. A Differential Theory of Radiative Transfer. *ACM Trans. Graph. (TOG)* **2019**, *38*, 1–16. [CrossRef]
55. Peraiah, A. *An Introduction to Radiative Transfer: Methods and Applications in Astrophysics, by Annamaneni Peraiah*; Cambridge University Press: Cambridge, UK, 2001; Volume 492, p. 2001. [CrossRef]
56. Rodgers, C.D. Characterization and Error Analysis of Profiles Retrieved from Remote Sounding Measurements. *J. Geophys. Res. Atmos.* **1990**, *95*, 5587–5595. [CrossRef]
57. Eriksson, P.; Jiménez, C.; Buehler, S.A. Qpack, a General Tool for Instrument Simulation and Retrieval Work. *J. Quant. Spectrosc. Radiat. Transf.* **2005**, *91*, 47–64. [CrossRef]
58. Anderson, G.P.; Berk, A.; Chetwynd, J.H.; Harder, J.; Fontenla, J.M.; Shettle, E.P.; Saunders, R.; Snell, H.E.; Pilewskie, P.; Kindel, B.C.; et al. Using the MODTRAN5 Radiative Transfer Algorithm with NASA Satellite Data: AIRS and SORCE. In Proceedings of the Algorithms and Technologies for Multispectral, Hyperspectral, and Ultraspectral Imagery XIII, Orlando, FL, USA, 9–12 April 2007; SPIE: Washington, DC, USA, 2007; Volume 6565, pp. 590–600.
59. Strow, L.L.; Tobin, D.C.; Hannon, S.E. A Compilation of First-Order Line-Mixing Coefficients for CO2Q-Branches. *J. Quant. Spectrosc. Radiat. Transf.* **1994**, *52*, 281–294. [CrossRef]
60. Niro, F.; Jucks, K.; Hartmann, J.-M. Spectra Calculations in Central and Wing Regions of IR Bands. IV: Software and Database for the Computation of Atmospheric Spectra. *J. Quant. Spectrosc. Radiat. Transf.* **2005**, *95*, 469–481. [CrossRef]
61. Adler-Golden, S.; Schweitzer, E.; Steinfeld, J. Ultraviolet Continuum Spectroscopy of Vibrationally Excited Ozone. *J. Chem. Phys.* **1982**, *76*, 2201–2209. [CrossRef]
62. Berk, A.; Conforti, P.; Hawes, F.; Perkins, T.; Guiang, C.; Acharya, P.; Kennett, R.; Gregor, B.; Bosch, J. *Next Generation MODTRAN for Improved Atmospheric Correction of Spectral Imagery*; Spectral Sciences, Inc.: Burlington, VT, USA, 2016.
63. Anderson, G.P.; Berk, A.; Chetwynd, J.H., Jr.; Harder, J.; Fontenla, J.M.; Shettle, E.P.; Saunders, R.; Snell, H.E.; Pilewskie, P.; Kindel, B.C.; et al. *Using the MODTRAN5 Radiative Transfer Algorithm with NASA Satellite Data: AIRS and SORCE*; Shen, S.S., Lewis, P.E., Eds.; NASA: Washington, DC, USA, 2007.
64. Eriksson, P.; Buehler, S.; Emde, C.; Sreerekha, T.; Melsheimer, C.; Lemke, O.; ARTS Theory. ARTS Development Team, Regularly Updated Versions. 2011. Available online: http://www.radiativetransfer.org/docs/ (accessed on 16 April 2018).
65. Niro, F.; Boulet, C.; Hartmann, J.-M. Spectra Calculations in Central and Wing Regions of CO2 IR Bands between 10 and 20 μm. I: Model and Laboratory Measurements. *J. Quant. Spectrosc. Radiat. Transf.* **2004**, *88*, 483–498. [CrossRef]
66. Niro, F.; Hase, F.; Camy-Peyret, C.; Payan, S.; Hartmann, J.-M. Spectra Calculations in Central and Wing Regions of $CO_2$ IR Bands between 10 and 20 μm. II. Atmospheric Solar Occultation Spectra. *J. Quant. Spectrosc. Radiat. Transf.* **2005**, *90*, 43–59. [CrossRef]
67. Millot, G.; Lavorel, B.; Steinfeld, J. Collisional Broadening, Line Shifting, and Line Mixing in the Stimulated Raman 2ν2 Q Branch of $CH_4$. *J. Chem. Phys.* **1991**, *95*, 7938–7946. [CrossRef]
68. Grigoriev, I.; Filippov, N.; Tonkov, M.; Gabard, T.; Le Doucen, R. Estimation of Line Parameters under Line Mixing Effects: The N3 Band of CH4 in Helium. *J. Quant. Spectrosc. Radiat. Transf.* **2001**, *69*, 189–204. [CrossRef]